

BOLOMETRIC FLUX ESTIMATION FOR COOL EVOLVED STARS

GERARD T. VAN BELLE¹, MICHELLE CREECH-EAKMAN², ALMA RUIZ-VELASCO¹

Accepted for Publication in AJ

ABSTRACT

Estimation of bolometric fluxes (F_{BOL}) is an essential component of stellar effective temperature determination with optical and near-infrared interferometry. Reliable estimation of F_{BOL} simply from broad-band K -band photometry data is a useful tool in those cases where contemporaneous and/or wide-range photometry is unavailable for a detailed spectral energy distribution (SED) fit, as was demonstrated in Dyck et al. (1974). Recalibrating the intrinsic F_{BOL} versus observed $F_{2.2\mu\text{m}}$ relationship of that study with modern SED fitting routines, which incorporate the significantly non-blackbody, empirical spectral templates of the INGS spectral library (an update of the library in Pickles 1998) and estimation of reddening, serves to greatly improve the accuracy and observational utility of this relationship. We find that F_{BOL} values predicted are roughly 11% less than the corresponding values predicted in Dyck et al. (1974), indicating the effects of SED absorption features across bolometric flux curves.

Subject headings: stars: fundamental parameters (radii, temperatures); stars: distances; stars: carbon; instrumentation: high angular resolution; instrumentation: interferometers; infrared: stars

1. INTRODUCTION

A substantial number of angular sizes of cool, evolved stars have been measured over the past two decades with increasingly sophisticated optical interferometry facilities operating in both the near-infrared (taken here to be 1.0–2.5 μm) and the optical (0.3–1.0 μm). However, without ancillary measurements, these apparent sizes (θ) are of limited utility. When combined with distance (d), a linear size may be obtained; when combined with a measurement of bolometric flux (F_{BOL}), the effective temperature (T_{EFF}) may be measured. The latter comes from the definition of luminosity (L), relating it to stellar radius R and T_{EFF} (and the usual mathematical / physical constants):

$$L = 4\pi\sigma R^2 T_{\text{EFF}}^4 \quad (1)$$

Dividing both sides by d reduces this to the relationship:

$$T_{\text{EFF}} = 2341 \left(\frac{F_{\text{BOL}}}{\theta_R} \right)^{1/4} \quad (2)$$

where the Rosseland angular size θ_R is in units of milliarcseconds (mas), and F_{BOL} is given as 10^{-8} ergs cm^{-2} sec^{-1} ; the resultant T_{EFF} is in Kelvin (K). The Rosseland mean angular size is the wavelength-averaged angular size incorporating the wavelength-weighted Rosseland mean opacity – effectively, the mean radiating surface of the star (definitional discussions can be found in Seaton et al. 1994; Seaton & Badnell 2004). The value for F_{BOL} is to be taken as the flux arriving at Earth from the observed star, assuming no intervening extinction between it and the observer.

Unfortunately, many interferometric size determinations are not done in direct conjunction with matching

measures of d or F_{BOL} . In the case of distance, this (relatively) invariant parameter can be measured long after (or before) the corresponding measure of θ takes place, with no significant effect upon the ultimately determined linear size, R .

For bolometric flux, the situation is more challenging. Complete characterizations of the total flux output from the shortest to longest wavelengths are rarely done for most objects, and even simple photometry is rarely carried out at the time of the interferometric observations. Many of the coolest objects that are of particular interest to interferometry vary in brightness substantially on time periods short compared to the lag between flux and size measurements. For the bandpasses where they are brightest – in the near-infrared – instrumentation tends to be available only on larger telescopes, meaning these objects saturate detectors and fall squarely in a surprising ‘blind spot’ of modern astronomy. To complicate matters further, many of these objects are distant, which means a correction for interstellar reddening must be taken into account as well. An important piece of the solution is the fact that interferometers typically collect measurements of the incoherent flux levels³ at their wavelengths of operations – typically K -band – in addition to measures of interference during their observations.

Historically, effective use of these data was directly affected by the advent of useful infrared detectors in the 1960’s, which resulted in the seminal Two Micron Sky Survey (Neugebauer & Leighton 1969) and the dissertation work of Wing (1967). The ensuing work by Dyck et al. (1974, hereafter DLC74) demonstrated relationships between band-to-bolometric flux ratios and spectral type, at 0.55, 1.04, and 2.2 μm (see Figure 6 of DLC74 in particular), for ‘relatively normal’ Mira variables and giants. Spectral types in the DLC74 study were determined contemporaneously to account for this parameter appearing to change with variable star phase.

³ The light at the end of the tunnel, as it were.

¹ Lowell Observatory, 1400 W. Mars Hill Rd., Flagstaff, Arizona, USA; gerard@lowell.edu, alma@lowell.edu

² New Mexico Institute of Mining & Technology, 801 Leroy Pl., Socorro, NM 87801; mce@kestrel.nmt.edu

For the $F_{1.04\mu\text{m}}/F_{\text{BOL}}$ ratio, the relationship was essentially flat for spectral types M0 through \sim M6; for $F_{2.2\mu\text{m}}/F_{\text{BOL}}$, the ratio changes slowly and in a linear fashion from M0 all the way out to M10.

However, with a number of recent advances, the specific results of DLC74 bear a revisit and recalibration. The spectral template library of Pickles (1998) allows for a much more fine-grained fitting of spectral energy distributions to the the photometry present in DLC74 - e.g. see Figures 1-3 in that paper, which effectively does a simple Riemann sum as a function of wavelength to determine their values for F_{BOL} . Such a sum approximates a blackbody curve, and does not account for absorption features present between photometric bands - which, particularly for the later-type stars, can be considerable (non-)contributions of the stellar spectral energy distribution (SED) curve. Current sophisticated SED fitting codes can make use of the unreddened Pickles templates, constrain them by the photometry in DLC74 - which remain high-quality measurements - and also incorporate reddening corrections.

2. PHOTOMETRY AND DATA REDUCTION

2.1. Targets and Photometric Data

The target data come from 84 observations of 60 objects found in DLC74, all of which are cool evolved stars at spectral types M4.0III and later. Two objects have measurements at 4 separate epochs, three objects have 3 epochs, and 11 have 2 epochs. These 60 objects include contemporaneous flux measurements in $\log F_{\lambda}$ (in $\text{W cm}^{-2} \mu\text{m}^{-1}$) across up to 12 bands from $0.55\mu\text{m}$ to $10.2\mu\text{m}$, along with epoch-specific spectral type determinations for 70 of the 84 observations, and 34 F_{BOL} determinations. Broad-band filters representing the *V*, *J*, *H*, *K*, *L*, *M*, and *N* passbands were used, along with narrowband filters at 0.78, 0.87, 0.88, 1.04 and $1.05 \mu\text{m}$ with filter-specific properties listed in Table 1. Further details on the narrowband system can be found in DLC94, along with Lockwood & Wing (1971); Lockwood (1972, 1973); Wing & Lockwood (1973).

TABLE 1
PROPERTIES OF THE LOCKWOOD & WING (1971) PHOTOMETRIC SYSTEM.

Designation	Central wavelength (\AA)	Width at half power (\AA)	Feature Measured
78	7817	90	TiO
87	8778	82	Continuum (TiO after M5)
88	8884	114	TiO
104	10351	125	Continuum
105	10506	100	VO

For the purposes of this study, we have taken the data in DLC74 and converted it into Janskys (Jy), which can be found in Table 2. Spectral types listed in this table for each of the stars were determined contemporaneously by DLC74 using the TiO and VO band strengths in the narrowband photometry, using the T_1 , T_2 , V_1 , D color indices calibration and technique found in Lockwood (1972). The color indices found in Lockwood (1972) were used to type stars in integer subtypes between M1 and M3, half-

integer subtypes between M4.0 and M8.0, and quarter-integer subtypes between M8.0 and M10.

DLC74 cite their photometry errors as “2-3 percent” for their narrowband data, “5 percent or less” for 1-4 μm , and “10 percent or slightly greater” for their 5 and 10.2 μm data points; no error is given for *V*-band data, except to note that their stars are “extremely faint” (and imply that larger errors result). From the numerical modeling presented in the next section, this appears to correspond to a median measurement values of $\lesssim 10^{-9} \text{ W cm}^{-2} \mu\text{m}^{-1}$. In practice, we found that inflating these errors by a factor of $2\times$ was necessary to achieve average reduced χ^2 values approaching 1.0 in the next section. We additionally found that for the latest type stars ($>M7.5\text{III}$), data from the 3 shortest wavelength filters was also “extremely faint” (also $\lesssim 10^{-9} \text{ W cm}^{-2} \mu\text{m}^{-1}$) and that 2-3% errors for these data were underestimates.

2.2. Spectral Energy Distribution Fitting with sedFit

For SED fitting, we used the `sedFit` code that we have employed on previous occasions (e.g. van Belle et al. 2007, 2008; van Belle & von Braun 2009) for determination of bolometric flux and other relevant stellar parameters. The flux data from DLC74 were matched against a grid of M-giant template spectra; for comparison, the epoch-specific spectral types determined in DLC74 were also specifically evaluated.

The template spectra were based upon the INGS (IUE / NGSLS / SpeX) library of Pickles⁴, an update of the earlier catalog of Pickles (1998). The INGS combines IUE data (Heck et al. 1984), NGSL data (Heap & Lindler 2011), and SpeX data (Rayner et al. 2009) to produce a compendium of 143 stellar spectra, and significantly improves the late-type spectra relative to Pickles (1998). This is primarily due to the later spectra being now observationally based, in contrast to Pickles (1998) which used the theoretical spectra from Fluks et al. (1994) for the late M giant spectra. A search grid was developed from the 11 subtype templates found in the INGS between M0III and M10III, with half-subtypes generated by interpolating between those 11 templates. This grid of these spectra were searched by chi-squared minimization by fitting, for each template, the bolometric flux level F_{BOL} and wavelength-dependent reddening. For all but 3 of the 84 flux data sets, a slightly different spectral subtype from the grid search fit better than the indicated DLC74 spectral type; typically this was roughly one subtype bluer than DLC74.

In combination with an effective temperature estimate that assigned to each spectral type (based upon the values in - interpolated or extrapolated where necessary - van Belle et al. 1999), an estimate of the angular sizes of these objects was produced as a potentially useful secondary data product. Reddening corrections were based upon the empirical reddening determination by Cardelli et al. (1989), which differs little from van de Hulst’s theoretical reddening curve No. 15 (Johnson 1968; Dyck et al. 1996). Zero-magnitude flux density calibrations for broadband photometry data points were based upon the values given in Fukugita et al. (1995) and Cox (2000). In contrast to similar earlier SED efforts of

⁴ <http://lcogt.net/user/apickles/dev/INGS/>

ours, no literature photometry (such as Stromgren *ubvy* β or 2MASS data in Rufener 1976; Cutri et al. 2003) was utilized herein, given the non-contemporaneous nature of those data sets.

The *V*-band data were not used in the SED fitting for a number of reasons. Principally, the more variable stars (e.g. the Miras) have variations in T_{EFF} and R , and dust production which causes up to 8 magnitudes of variation in *V*, rendering data in this bandpass useless for SED fitting. Additionally, the weighting on the data points was unclear given the non-numerical quantification of the signal-to-noise in DLC74. As such, the *V* data had a disproportionate effect in determination of reddening, even when given low statistical weight. Determination of reddening was still well-characterized for these stars given the inclusion of the shorter-wavelength narrow-band filters (LW 78, 87, 88). For determination of the intrinsic bolometric flux (F_{BOL}) below, it is important to be as unbiased as possible in characterizing reddening. Contributions longwards ($\lambda > 2.5\mu\text{m}$) of the data presented in the template spectra were estimated via a Rayleigh-Jeans tail and typically were a minor ($< 10\%$) contribution.

The results from the SED fitting can be seen in Table 3, including estimates for reddening, angular size, and bolometric flux. The full set of summary `sedFit` output plots can be seen in the Appendix in Figures A1-A14. Six objects had abnormally large χ^2 per degree-of-freedom values ($\chi^2_{\nu} > 6$) and were not considered in the ensuing analyses. Unsurprisingly, four of these six (IRC-10236, IRC+40485, IRC+50096, IRC+50357) are those objects noted in DLC74 as carbon stars; the remaining two (IRC+40004, IRC+40448) are M-type in DLC74 but had sufficiently spurious fits that they were set aside. Interestingly, all objects designed in DLC74 as S-type (R And, R Cam, R Cyg) had SED fits with reasonable χ^2_{ν} values indistinguishable from the M-type stars.

For the remaining objects the χ^2_{ν} values for the SED fits have a median value of $\simeq 0.64$, with a maximum of 2.4.⁵ All χ^2_{ν} values are based upon employing the error bars discussed at the end of §2.1. There is a correlation between these χ^2_{ν} values, seen in Figure 1, with a significant increase in χ^2_{ν} for the redder stars, beginning at M7.5III. Similarly, we see an increase in the range of reddening fit values in Figure 2 for the later spectral types, also beginning at M7.5III, and possibly one-half subtype earlier. However, considering A_V versus χ^2_{ν} (Figure 3), there is quite a bit of scatter between these parameters.

Taken together, Figures 1, 2, and 3 lead us to the following conclusions: first, the spectral type templates of the Pickles INGS are somewhat problematic for spectral types around M8III, for those bandpasses found in the narrowband filters of Lockwood & Wing (1971). Second, increasing values of A_V for the later spectral types are associated with increasing amounts of circumstellar, rather than interstellar, dust, given the known increase in mass loss rates with increasing spectral type (Dupree 1986; Guandalini 2010). Third, the slight trend in A_V versus χ^2_{ν} towards increasing A_V for $\chi^2_{\nu} > 1$ indicates

⁵ An earlier investigation utilizing the Pickles (1998) templates in like manner to the INGS templates had median values of $\chi^2_{\nu} \simeq 4$, with a significant increasing trend in χ^2_{ν} versus spectral subtype; it is on this basis that we find that the INGS templates are significantly better for the later subtypes.

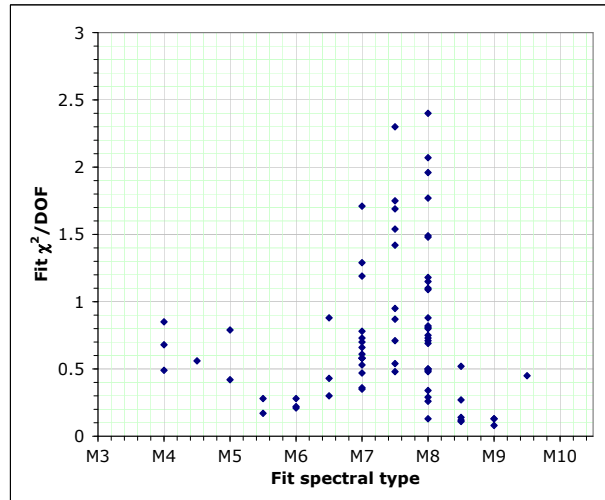


FIG. 1.— The reduced χ^2 (χ^2_{ν}) of each SED fit versus spectral type.

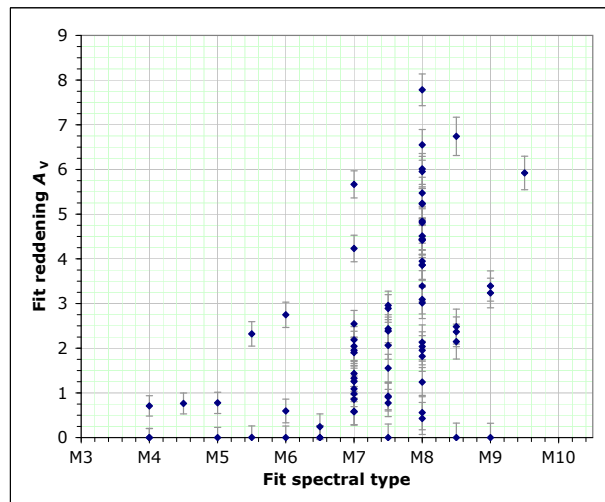


FIG. 2.— The reddening A_V of each SED fit versus spectral type.

that poorness of fit – potentially due to a lack of sufficient granularity in the INGS spectral template grid – might result a increased value for A_V .

Objects with Anomalous Results. As noted above, a number of objects explicitly identified as carbon stars were presented in DLC74 (IRC-10236, IRC+40485, IRC+50357, IRC+50096), and fits using M10III templates were attempted, under the notion that these latest spectral types would be most analogous to the carbon stars. However, as seen in the summary plots in the Appendix, this approach failed: SEDs for these object exhibit a distinctive, almost linear increase in flux with increasing wavelength. Additionally, stars IRC+40004, and IRC+40448 were assigned M-type subtypes in DLC74 (M9III, and M7III, respectively) but exhibited photometry reminiscent of the carbon star phenomenon. None of these objects that exhibited carbon behavior were included in Figures 1-3 or utilized in the discussion of §3. A cursory attempt was made to compare the data to model SED templates for the carbon stars (e.g. Aringer et al. 2009), but this was not successful; fits to carbon star SEDs remain an interesting and involved challenge (e.g. see extensive discussion in the

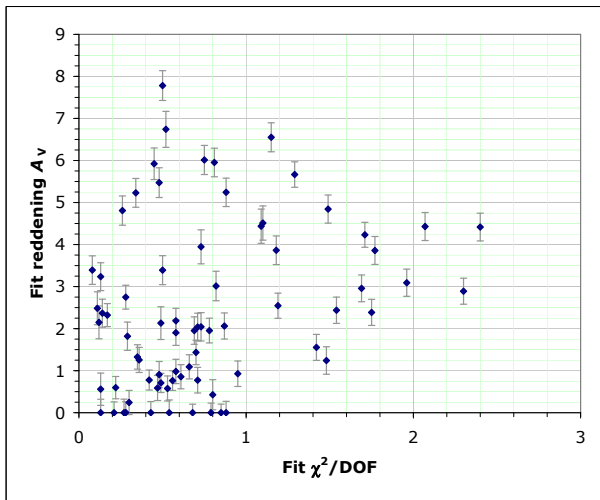


FIG. 3.— The reddening A_V of each SED fit versus reduced χ^2 (χ^2_ν). recent work by Rau et al. 2015).

3. DISCUSSION

3.1. Bolometric Flux Relationships

As inspired by DLC74 (particularly Figure 6 in that article), we examined the intrinsic bolometric flux (F_{BOL}) versus observed $2.2 \mu\text{m}$ flux ($F_{2.2\mu\text{m}}$) in Figure 4, and found the simple relationship fit:

$$F_{\text{BOL}} = F_{2.2\mu\text{m}} \times (3.340 \pm 0.101) - (0.04 \pm 0.33) \times 10^{-8} \quad (3)$$

in $\text{erg cm}^{-2} \text{s}^{-2}$, with a reduced χ^2 of 1.66. Direct comparison of this fit for F_{BOL} against the values from the SED fitting indicates a median intrinsic scatter of this relationship, across the range of bolometric fluxes in question, of 17%. It is important to emphasize that this is the relationship between *observed* $2.2 \mu\text{m}$ flux versus *intrinsic* bolometric flux – the influence of reddening is considered in transforming from $F_{2.2\mu\text{m}}$ to F_{BOL} using this relationship. As such, this is a relationship of significant observational utility, but of limited value for understanding the underlying astrophysics.

We can leverage the estimate for A_V found in Table 3 to “correct” the observed $2.2\mu\text{m}$ flux for the intrinsic $2.2\mu\text{m}$ flux ($F_{2.2\text{corr},\mu\text{m}}$), which modifies the previous relationship to:

$$F_{\text{BOL}} = F_{2.2\text{corr},\mu\text{m}} \times (2.996 \pm 0.093) + (0.46 \pm 0.34) \times 10^{-8} \quad (4)$$

in $\text{erg cm}^{-2} \text{s}^{-2}$, with a reduced χ^2 of 1.55; as expected, this decreases the slope of the linear fit – the amount of intrinsic $2.2\mu\text{m}$ flux relative to the overall intrinsic bolometric flux is greater than the reddening-decreased apparent $2.2\mu\text{m}$ flux.

3.2. Comparison to DLC74

The intent of this investigation is to expand and update the intrinsic F_{BOL} versus $F_{2.2\mu\text{m}}$ relationship presented in DLC74. In particular, the use of specific Pickles INGS spectral templates, with the inclusion of significant absorption bands, along with an estimate of reddening, is expected to refine the values obtained for F_{BOL} . Inspection of how the fits compare to data in DLC74 is warranted before examining that derived quantity. The most

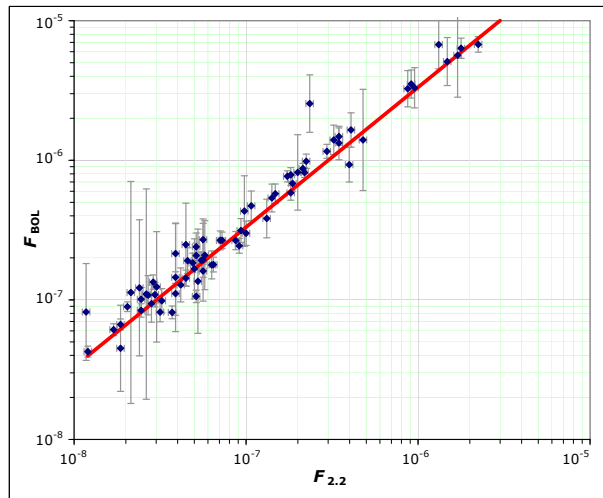


FIG. 4.— Intrinsic bolometric flux (F_{BOL}) versus observed $2.2 \mu\text{m}$ flux ($F_{2.2\mu\text{m}}$), in $\text{ergs cm}^{-2} \text{s}^{-1}$. The functional form of the red fit line is presented in Equation 3.

direct comparison is that of spectral type. DLC74 determined their spectral types by referencing the Lockwood & Wing narrowband fluxes against the color calibrations of Lockwood (1972); spectral types in this investigation were fixed to those values.

For completeness, we also explored fitting the photometry data for each star against subtypes fixed to those types found in DLC74. We found significantly poorer χ^2_ν values (as seen in Table 3) for these types which were, on average, 1 subtype later than the template found from searching a grid of INGS templates. Interestingly, the resultant F_{BOL} values were still comparable between fits using a DLC74-fixed subtype, versus a grid fitted subtype value, differing only at the $\sim 6\%$ level.

Overall, the inclusion of reddening in our SED fitting has the effect of increasing the indicated intrinsic F_{BOL} on a star-by-star basis, when the extinguishing effect of that phenomenon is taken into account. The competing effect of major near-infrared ‘gaps’ (due to absorption features in the spectra) in the SED leading to a lower integrated F_{BOL} relative to a F_{BOL} obtained from a simple Riemann sum (cf. consider the areas under the curve of our summary `sedFit` figures in the Appendix, and Figures 1, 2, or 3 of DLC74) will diminish the indicated F_{BOL} . This second effect should increase for increasingly redder spectral types, and this is borne out by examination of the ratio of DLC74 F_{BOL} values versus those determined herein (Figure 5). A fit to these data points gives

$$r = (-0.095 \pm 0.062) \times ST + (1.58 \pm 0.47) \quad (5)$$

with a reduced $\chi^2 = 0.30$; where r is the F_{BOL} ratio, $r = F_{\text{BOL,DLC74}}/F_{\text{BOL,sedFit}}$, and ST the M-class spectral subtype value; not every star in the previous figures is seen in this plot, because DLC74 did not provide a $F_{\text{BOL,DLC74}}$ for every one of their stars.

A separate way of looking at the effects of reddening and near-infrared absorption is to compare directly the derived F_{BOL} values from DLC74 and our work (Figure 6). Fitting for the relationship between the two sets

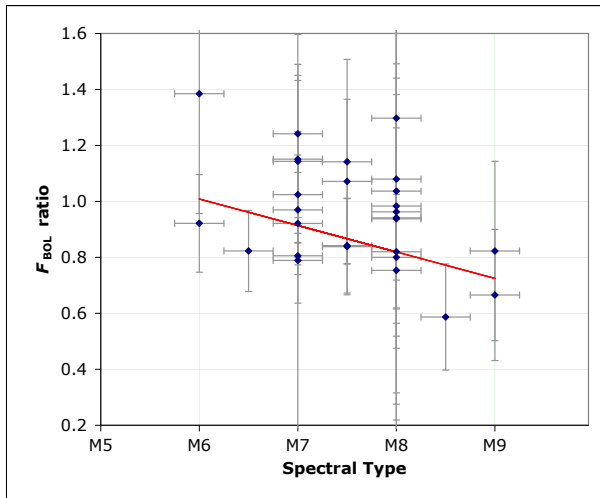


FIG. 5.— Ratio of F_{BOL} values for those values given in DLC74, versus the F_{BOL} values determined herein, as a function of M-class spectral subtype.

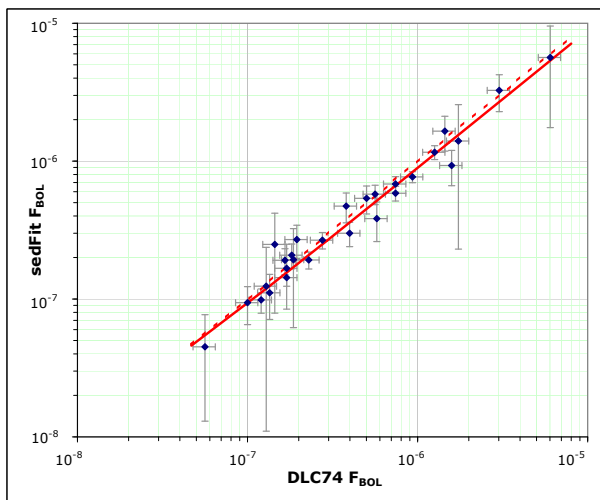


FIG. 6.— F_{BOL} as determined in this work by SED fitting, versus the values in DLC74. The red dotted line is the 1-to-1 correspondence line, while the red solid line is the line fit (Equation 6).

of values gives:

$$F_{\text{BOL, sedFit}} = (0.89 \pm 0.08) \times F_{\text{BOL, DLC74}} + (0.44 \pm 1.69) \times 10^{-8} \quad (6)$$

in units of $\text{ergs cm}^{-2} \text{s}^{-1}$ with a χ^2_{ν} of 0.39. On average, our F_{BOL} values are $\simeq 11\%$ lower than those found in DLC74.

3.3. Further Improvement upon Empirical Determination of F_{BOL}

As seen in DLC74, a second-order correction to the relationship between observed $2.2\mu\text{m}$ flux and overall intrinsic F_{BOL} can be considered. For DLC74, they present this as a weak spectral-type dependency (see their Figure 6 and discussion in §V.a). Unfortunately, in the notional observational scenario we are considering – angular size measurements contemporaneous with only K -band, and possibly V -band, measurements – contemporaneous spectral typing is not available. As such, development of a modern refinement of such a relationship seems of limited utility, particularly given the complications of spec-

tral type discussed in §3.2.

Instead of spectral type, a more directly quantitative index such as $\log F_{0.55\mu\text{m}}/F_{2.2\mu\text{m}}$ can be considered. However, a cursory examination of the ratio of $\log F_{\text{BOL}}/F_{2.2\mu\text{m}}$ to $\log F_{0.55\mu\text{m}}/F_{2.2\mu\text{m}}$ shows no significant improvement in determination of F_{BOL} over the 17% uncertainty found for Equation 3 – which provides no motivation for the complication introduced by now levying a requirement for contemporaneous V -band data in conjunction with the K -band data.

Incorporating our SED fitting A_V fit values into this analysis, to index with unreddened values, i.e. $\log F_{\text{BOL}}/F_{2.2\mu\text{m, corr}}$ versus $\log F_{0.55\mu\text{m, corr}}/F_{2.2\mu\text{m, corr}}$, shows a reduction in the predictive uncertainty for F_{BOL} decreasing to $\simeq 9\%$. While this is a significant improvement, it is a rather unrealistic one, presuming some knowledge of A_V which is not obtained without the complication of (and requirements for contemporaneous observational data over a wide bandpass) a full SED fit.

3.4. Empirical (non-)Determination of T_{EFF}

While this investigation has emphasized determination of F_{BOL} , we do not see it of direct utility in determining effective temperature (T_{EFF}). As noted in §2.2, a (T_{EFF}) is assigned to each spectral template, based upon the earlier calibration found in van Belle et al. (1999); this enabled an estimate of angular size to be derived from this SED fitting exercise. A recalibration of the (T_{EFF}) versus spectral type (or other index, such as $V-K$ color) would be useful and is in fact part of a larger effort on the part of the authors. However, the necessary new information – namely direct measures of angular sizes for highly evolved stars – will be part of a forthcoming publication; as such, any (T_{EFF}) recalibration is deferred until that investigation. This investigation directly enables that work by providing the photometrically-based determination of F_{BOL} for Equation 2.

4. CONCLUSIONS

Evaluation of the photometric data of DLC74 with current computing techniques, against empirical spectral templates, makes considerable utility of this still-impressive dataset. Refinement of the intrinsic F_{BOL} versus observed $F_{2.2\mu\text{m}}$ relationship, first noted in DLC74, provides observers with a useful tool in deducing the fundamental stellar parameter of T_{EFF} of these stars, even with limited observational data. This approach has considerable merit in further application against other early but high-quality photoelectric photometry, such as the extensive Wing (1967) data set.

Acknowledgements. This work would not have been possible without the `sedFit` code written by Andy Boden, and his generous technical support on the use thereof. We have made extensive use of the SIMBAD database and the VizieR catalogue access tool, operated by the CDS in Strasbourg, France (Ochsenbein et al. 2000). This research has made use of the AFOEV database, operated at CDS, France, and the GCPD database at the University of Lausanne, Switzerland (Mermilliod et al. 1997). This research has made use of NASA’s Astrophysics Data System.

Helpful input for this article resulted from discussions with and feedback from Wes Lockwood and Kaspar

von Braun. Funding for this research has been generously provided in part by Lowell Observatory and CONACyT, Mexico. This material is based upon work supported by

the National Science Foundation under Grant No. AST-1212203, and NASA Grant No. NNX13AF01G.

REFERENCES

- Aringer, B., Girardi, L., Nowotny, W., Marigo, P., & Lederer, M. T. 2009, *A&A*, 503, 913
- Cardelli, J. A., Clayton, G. C., & Mathis, J. S. 1989, *ApJ*, 345, 245
- Cox, A. N. 2000, *Allen's astrophysical quantities* (Allen's astrophysical quantities, 4th ed. Publisher: New York: AIP Press; Springer, 2000. Edited by Arthur N. Cox. ISBN: 0387987460)
- Cutri, R. M., Skrutskie, M. F., van Dyk, S., Beichman, C. A., Carpenter, J. M., Chester, T., Cambresy, L., Evans, T., Fowler, J., Gizis, J., Howard, E., Huchra, J., Jarrett, T., Kopan, E. L., Kirkpatrick, J. D., Light, R. M., Marsh, K. A., McCallon, H., Schneider, S., Stiening, R., Sykes, M., Weinberg, M., Wheaton, W. A., Wheelock, S., & Zacarias, N. 2003, *2MASS All Sky Catalog of point sources*.
- Dupree, A. K. 1986, *ARA&A*, 24, 377
- Dyck, H. M., Benson, J. A., van Belle, G. T., & Ridgway, S. T. 1996, *AJ*, 111, 1705
- Dyck, H. M., Lockwood, G. W., & Capps, R. W. 1974, *ApJ*, 189, 89
- Fluks, M. A., Plez, B., The, P. S., de Winter, D., Westerlund, B. E., & Steenman, H. C. 1994, *A&AS*, 105
- Fukugita, M., Shimasaku, K., & Ichikawa, T. 1995, *PASP*, 107, 945
- Guandalini, R. 2010, *A&A*, 513, A4
- Heap, S. R. & Lindler, D. 2011, in *Astronomical Society of the Pacific Conference Series*, Vol. 448, 16th Cambridge Workshop on Cool Stars, Stellar Systems, and the Sun, ed. C. Johns-Krull, M. K. Browning, & A. A. West, 887
- Heck, A., Egret, D., Jaschek, M., Jaschek, C., & Battrick, B., eds. 1984, *ESA Special Publication*, Vol. 1052, IUE low dispersion spectra reference atlas. Part 1: Normal stars
- Johnson, H. L. *Interstellar Extinction*, ed. B. M. Middlehurst & L. H. Aller (the University of Chicago Press), 167
- Lockwood, G. W. 1972, *ApJS*, 24, 375
- 1973, *ApJ*, 180, 845
- Lockwood, G. W. & Wing, R. F. 1971, *ApJ*, 169, 63
- Mermilliod, J.-C., Mermilliod, M., & Hauck, B. 1997, *A&AS*, 124, 349
- Neugebauer, G. & Leighton, R. B. 1969, *Two-micron sky survey. A preliminary catalogue*
- Ochsenbein, F., Bauer, P., & Marcout, J. 2000, *A&AS*, 143, 23
- Pickles, A. J. 1998, *PASP*, 110, 863
- Rau, G., Paladini, C., Hron, J., Aringer, B., Groenewegen, M. A. T., & Nowotny, W. 2015, *ArXiv e-prints*
- Rayner, J. T., Cushing, M. C., & Vacca, W. D. 2009, *ApJS*, 185, 289
- Rufener, F. 1976, *A&AS*, 26, 275
- Seaton, M. J. & Badnell, N. R. 2004, *MNRAS*, 354, 457
- Seaton, M. J., Yan, Y., Mihalas, D., & Pradhan, A. K. 1994, *MNRAS*, 266, 805
- van Belle, G. T., Ciardi, D. R., & Boden, A. F. 2007, *ApJ*, 657, 1058
- van Belle, G. T., Lane, B. F., Thompson, R. R., Boden, A. F., Colavita, M. M., Dumont, P. J., Mobley, D. W., Palmer, D., Shao, M., Vasisht, G. X., Wallace, J. K., Creech-Eakman, M. J., Koresko, C. D., Kulkarni, S. R., Pan, X. P., & Gubler, J. 1999, *AJ*, 117, 521
- van Belle, G. T., van Belle, G., Creech-Eakman, M. J., Coyne, J., Boden, A. F., Akeson, R. L., Ciardi, D. R., Rykoski, K. M., Thompson, R. R., Lane, B. F., & PTI Collaboration. 2008, *ApJS*, 176, 276
- van Belle, G. T. & von Braun, K. 2009, *ApJ*, 694, 1085
- Wing, R. F. 1967, *PhD thesis*, University of California, Berkeley.
- Wing, R. F. & Lockwood, G. W. 1973, *ApJ*, 184, 873

APPENDIX

SEDFIT PLOTS

The summary spectral energy distribution fitting plots from *sedFit* for each of the stars discussed in §2.2 are presented in Figures A1-A14.

TABLE 2

OBSERVATIONAL DATA FOR THE PROGRAM STARS DERIVED FROM DLC74, INCLUDING SPECTRAL TYPES, BOLOMETRIC FLUX ($\text{LOG [W CM}^{-2}\text{)]}$), AND FILTER FLUXES (JY).

Star	JD 2440000+	Spectral Type	$\log F_{\text{BOL}}$	0.55 μm	78	87	88	104	105	1.25 μm	1.65 μm	2.2 μm	3.4 μm	5.0 μm	10.2 μm
IRC-30217	1050	M9.8	-14	0.0019	0.301	1.51	1.86	12.67	6.54		39.61	45.47	46.33		34.90
IRC-30217	1107	M9.3		0.0124	1.043	4.67	5.50	25.87	16.06			51.02	58.32	49.07	54.06
IRC-20293	1051	M7.9	-13.74	0.0580	1.813	8.91	8.71	29.71	28.56		99.51	82.74	59.68		10.07
IRC-10236	1049	c		0.0171	0.600	1.02	1.10	2.20	2.43		30.05	111.62	376.56		516.27
IRC+00028	1215	M7.9	-13.56	0.1752	3.702	18.18	16.60	52.83	50.79	94.78	137.36	116.88	76.88	40.81	31.11
IRC+00266	1050	M9.6	-14.25	0.0006	0.069	0.47	0.58	4.29	2.43		24.43	30.04	30.61		19.18
IRC+00266	1107	M9.9		0.0003	0.045	0.35	0.44	3.49	1.80			18.96	20.22		
IRC+00281	1049	M7.8		0.1158	2.446	11.21	10.47	32.57	32.04		97.24	79.02	47.41		
IRC+10011	1251					0.02		0.40	0.22	1.94	15.06	84.67	367.99		
IRC+10050	1277	M9.5		0.0450	7.053	39.78	50.13	373.98	221.69	655.69	1252.70	1540.72	2117.56		
IRC+10313	1215	M8.4		0.0206	0.756	3.80	3.72	16.32	13.67	32.11	53.44	47.61	33.56		
IRC+10523	1215	M9.1	-13.4	0.0298	2.082	10.46	10.97	56.60	37.65	103.92	157.71	161.33	153.40	138.30	220.23
IRC+10523	1251	M9.2		0.0211	1.543	8.12	8.91	54.06	34.34	94.78	150.61	150.57	143.16		
IRC+10525	1251	M8.5		0.0061	0.810	4.89	5.13	21.52	17.61	37.73	65.74	82.74	111.13		148.89
IRC+20052	1215	M8.1	-13.42	0.0820	2.873	14.44	13.81	54.06	49.63	116.60	189.60	172.87	124.69	76.00	41.01
IRC+20281	1109	M9.3		0.0006	0.043	0.28	0.34	2.53	1.61			42.43	78.67		87.68
IRC+20328	1106	M9.8		0.0030	0.406	2.24	2.75	19.63	10.61			92.84	116.37		87.68
IRC+30021	1106	M8.9		0.0016	0.287	1.78	1.95	11.56	8.43			62.77	75.13	67.74	138.96
IRC+30021	1214	M9.4	-13.89	0.125	0.69	0.87	6.07	3.76	16.47	39.61	48.72	58.32	89.29	126.73	
IRC+30021	1251	M9.6		0.0004	0.085	0.58	0.69	5.16	2.99	13.70	30.75	43.42	53.19		
IRC+30021	1277	M9.7		0.063	0.41	0.52	4.20	2.38	12.21	29.37	38.70	47.41			
IRC+30055	1215	M7.9	-13.78	0.0401	1.440	7.24	6.61	24.15	23.75	48.61	80.88	73.74	50.80	43.73	24.71
IRC+30292	1074	M8.6	-13.87	0.154	0.93	1.05	6.50	5.32			39.61	62.77	90.33	63.21	121.03
IRC+30292	1215	M9.6	-14.06	0.039	0.26	0.34	2.47	1.43	7.19	20.79	34.49	48.51	66.19	89.72	
IRC+30515	1215	M7.9	-13.25	0.2475	6.583	32.33	28.85	96.13	92.42	184.80	280.44	238.63	156.98	109.85	59.28
IRC+40004	1215		-13.51			0.13	0.15	2.10	1.61	14.34	52.22	99.48	176.13	295.68	460.13
IRC+40004	1251	M9.1		0.0006	0.011	0.13	0.15	1.67	1.19	10.88	43.44	84.67	149.91		290.32
IRC+40442	1251	M9.3		0.0045	0.548	3.39	4.07	27.09	16.82	71.90	147.18	157.66	133.61		49.30
IRC+40448	1215	M7.0	-12.63	0.059	0.50	0.48	3.18	3.60	14.34	82.76	361.18	1367.21	2635.23	6499.48	
IRC+40485	1215	c	-13.47	0.0175	0.791	1.55	1.74	3.83	4.22	11.66	41.48	106.59	211.76	363.76	304.00
IRC+40485	1251	c		0.0253	1.043	1.95	2.29	4.93	5.32	14.34	48.74	122.38	232.19		215.22
IRC+50096	1215	c	-13.13	0.0899	2.180	3.80	4.37	8.37	9.03	22.74	68.84	193.97	485.11	814.36	918.08
IRC+50096	1251	c		0.1056	2.282	4.17	4.68	9.18	10.37	26.10	80.88	222.70	556.98		
IRC+50260	1054	M7.0		0.2257	2.180	9.11	8.13	18.13	21.17			52.22	39.60	24.31	
IRC+50261	1078	M6.0		0.1712	2.682	9.54	8.71	16.70	17.61			34.50	27.40	19.31	
IRC+50357	1215	c	-13.83			0.05		0.15		0.84	5.34	22.79	88.27	209.32	200.85
IRC+60015	1251	M7.8		0.1392	3.224	16.21	14.79	44.96	45.26	84.47	131.17	114.22	75.13		18.74
IRC+60052	1251	M6.0		0.0985	2.940	12.29	11.75	27.72	29.91	52.08	92.86	82.74	58.32		21.03
IRC+60092	1215	M8.6	-13.24	0.477	3.55	3.80	23.60	19.31	59.80	143.83	212.68	299.11	408.15	799.61	
IRC+60169	1054	M9.3		0.0127	1.543	7.58	8.91	52.83	32.79		274.06	321.90	343.43		460.13
IRC+60184	1054	M8.8		0.0175	0.930	4.46	4.68	22.02	16.43		49.87	59.94	47.41		
IRC+60288	1106	M9.3		0.0040	0.435	3.09	3.47	23.06	14.31			67.25	62.49	47.95	33.33
IRC+60288	1214	M8.2	-13.64		2.873	15.48	14.79	42.94	36.79	62.62	95.03	88.66	82.38	66.19	68.06
IRC+60288	1251	M8.2		0.0430	2.446	13.79	13.49	42.94	36.79	65.57	111.65	104.17	92.44		
IRC+60289	1215	M7.9		0.0221	0.773	4.36	3.98	13.89	13.36	28.62	44.45	39.60	27.91	24.59	
IRC+60316	1215	M6.0	-13.71	0.0608	2.336	10.96	10.24	27.09	28.56	55.81	97.24	90.72	63.95	36.38	24.71
IRC+60334	1251	M8.9		0.0076	0.629	3.31	3.72	19.63	13.99	39.51	79.04	101.79	111.13		78.14
IRC+70102	1052	M9.0	-13.92	0.0111	0.791	3.71	4.07	18.74	12.47		54.68	52.21	50.80		39.16
IRC+70171	1215	M9.2	-13.73	0.0023	0.338	1.90	2.34	13.27	8.43	34.41	75.48	90.72	90.33	70.93	74.62
IRC+70171	1251	M9.3	-13.84	0.0016	0.262	1.44	1.82	10.54	6.54	23.81	58.59	72.06	71.75		62.07
IRC+80005	1050	M9.5		0.0011	0.181	1.44	1.78	12.38	7.34	32.86	61.35	62.77	51.98		
IRC+80005	1215	M9.2	-13.77	0.0007	0.294	2.24	2.34	15.59	9.90	45.36	79.04	80.86	66.96	51.38	24.15
R And	1214		-12.76	0.0878	7.386	35.45	38.91	138.95	156.95	443.30	790.40	772.19	717.52	603.70	680.58
R And	1277			0.0136	1.344	8.91	8.91	44.96	54.42	136.99	329.49	378.20	422.51		
W And	1215	M6.5	-12.8	1.2990	21.797	97.65	93.35	270.92	272.74	532.97	754.83	642.28	474.06	331.76	225.36
W And	1251	M7.9		0.2419	10.195	51.25	50.13	191.80	188.69	336.28		559.40	432.35		
W And	1277	M8.3		0.1056	5.351	29.49	31.63	145.49	124.67	386.10	572.59	522.06	412.89		
W And	1302	M8.9		0.0505	3.079	17.77	19.96	112.94	82.37			559.40	496.41		
T Aqr	1251	M8.0		0.0259	1.043	5.37	4.68	12.97	11.91	17.25	22.28	19.40	15.34		
T Ari	1214	M7.0	-12.9	1.3292	28.734	128.73	112.23	264.75	272.74	395.09	599.58	476.13	335.61	240.34	103.01
U Ari	1251	M9.5		0.0094	1.226	9.33	10.00	66.50	38.53	108.82	154.12	140.52	136.72		
U Ari	1277			0.0164				79.95	46.32	111.35	161.38	147.14	133.61		
R Boo	1078	MB.1		0.0783	2.621	16.21	14.79	51.62	45.26		109.11	90.72	70.12		
R Cam	1078			0.3417	8.287	16.21	17.38	27.09	29.22		62.78	46.53	32.05		
R Cas	1214	M9.3	-12.22	0.1635	16.159	89.06	104.74	606.52	367.92	1537.09	2617.26	2739.83	2487.92	1999.03	2008.53
R Cas	1251	M9.7		0.0783	9.737	54.91	69.20	481.77	260.47	1015.54	1896.04	2126.79	1931.24		1078.65
R Cas	1302	M9.9		0.0783	8.480	45.67	56.25	449.62	232.14			2386.29	2545.87		
T Cas	1214	M8.9	-12.52	0.1131	10.676	66.02	70.81	373.98	260.47	905.10	1506.08	1405.15	1061.30	742.71	481.81
T Cas	1251	M8.7		0.1752	14.737	89.06	95.52	481.77	367.92	1039.20	1577.05	1471.38	1163.69		325.75
V Cas	1214	M7.9	-13.13	0.3263	8.880	48.94	44.68	142.18	136.70	249.29	361.28	300.42	221.74	135.15	62.07
Y Cas	1214	MB.1	-13.13	0.3496	11.979	48.94	47.87	138.95	121.83	202.63	307.50	293.58	254.59	195.35	170.95
SS Cas	1277	M4.0		1.2405	8.287	16.97	16.60	22.53	24.31	29.97	39.61	32.94	25.46		
T Cep	1214	M8.6		0.8782	42.501	251.00	251.24	1210.16	924.17	2273.52	3371.68	2868.96	2117.56		
R Cyg	1214			1.9213	45.541	87.03	93.35	159.53	164.34	255.09	353.06	293.58	254.59		
X Cyg	1214	M8.2		0.4504	49.935	467.38	398.20	1632.46	1431.38	2671.15	3696.98	3611.80	3434.29		
S Lac	1251	M8.2	-13.77	0.0517	1.653	8.12	8.13	32.57	28.56	57.11	79.04	72.06	53.19		12.67
R Leo	1109										15770.54	122383.85	10135.30	5634.02	3333.33
W Lyr	1214	M6.5		0.1835	2.682	10.23	9.12	18.74	18.87	26.10	36.13	30.04	23.76		
V Mon	1277	M5.0		2.9081	39.665	114.73	109.67	200.84	211.72	313.83	454.83	361.18	266.59		
R Tri	1214	M5.0	-13												

TABLE 3

SPECTRAL ENERGY DISTRIBUTION FITTING RESULTS, INCLUDING FIT SPECTRAL TYPE, χ^2_{DOF} FOR BOTH DLC74 AND OUR SPECTRAL TYPE, ESTIMATES FOR REDDENING (A_V , IN MAG), ANGULAR SIZE (θ_{EST} , IN MAS), AND FIT BOLOMETRIC FLUX AS COMPARED TO DLC74 FLUX (F_{BOL} , IN $\text{ERG S}^{-1} \text{CM}^{-2}$).

Star	JD 2440000+	SED Fitting Results						F_{BOL}	DLC74 F_{BOL}
		DLC74 SpType	Fit SpType	DLC74 χ^2/DOF	Fit χ^2/DOF	A_V (mag)	θ_{EST}		
IRC-30217	1050	M9.8	M8III	428.16	0.82	3.01 ± 0.35	1.81 ± 0.31	(9.41 ± 2.89) × 10 ⁻⁸	1.00 × 10 ⁻⁷
	1107	M9.3	M8III	549.87	0.13	0.56 ± 0.38	1.69 ± 0.18	(8.17 ± 1.30) × 10 ⁻⁸	
IRC-20293	1051	M7.9	M7III	33.41	0.58	1.90 ± 0.30	2.52 ± 0.32	(2.08 ± 0.42) × 10 ⁻⁷	1.82 × 10 ⁻⁷
IRC-10236	1049	c	M2III	355.15	18.15	8.81 ± 0.40	2.46 ± 6.92	(4.73 ± 0.27) × 10 ⁻⁷	
IRC+00028	1215	M7.9	M7III	31.44	0.58	0.98 ± 0.29	2.85 ± 0.29	(2.67 ± 3.63) × 10 ⁻⁷	2.75 × 10 ⁻⁷
IRC+00266	1050	M9.9	M8III	421.87	0.48	5.47 ± 0.35	1.69 ± 0.69	(8.19 ± 0.66) × 10 ⁻⁸	
	1107	M9.6	M8III	298.95	1.10	4.51 ± 0.41	1.26 ± 0.46	(4.50 ± 0.32) × 10 ⁻⁸	5.62 × 10 ⁻⁸
IRC+00281	1049	M7.8	M7III	41.11	0.36	1.26 ± 0.30	2.36 ± 0.26	(1.84 ± 0.29) × 10 ⁻⁷	
IRC+10011	1251	M8.5	M9.5III	319.69	0.45	5.92 ± 0.38	2.43 ± 1.07	(1.36 ± 0.12) × 10 ⁻⁷	
IRC+10050	1277	M9.5	M8III	405.86	0.50	3.39 ± 0.34	10.76 ± 1.95	(3.31 ± 1.10) × 10 ⁻⁶	
IRC+10313	1215	M8.4	M7.5III	11.12	0.87	2.06 ± 0.31	1.88 ± 0.23	(1.09 ± 0.22) × 10 ⁻⁷	
IRC+10523	1215	M9.2	M8III	11.87	0.69	1.95 ± 0.33	3.31 ± 0.40	(3.14 ± 0.62) × 10 ⁻⁷	
	1251	M9.1	M8III	9.46	0.71	2.04 ± 0.33	3.24 ± 0.40	(3.00 ± 0.60) × 10 ⁻⁷	3.98 × 10 ⁻⁷
IRC+10525	1251	M8.5	M9III	2.70	0.13	0.00 ± 0.32	2.07 ± 0.18	(1.06 ± 0.11) × 10 ⁻⁷	
IRC+20052	1215	M8.1	M7III	25.20	1.19	2.55 ± 0.30	3.79 ± 0.54	(4.72 ± 1.15) × 10 ⁻⁷	3.80 × 10 ⁻⁷
IRC+20281	1109	M9.3	M8.5III	157.80	0.52	6.74 ± 0.43	2.03 ± 1.77	(1.10 ± 0.19) × 10 ⁻⁷	
IRC+20328	1106	M9.8	M8III	450.70	0.73	3.95 ± 0.40	2.70 ± 0.80	(2.09 ± 0.12) × 10 ⁻⁷	
IRC+30021	1106	M9.6	M8.5III	272.57	0.11	2.48 ± 0.39	2.01 ± 0.36	(1.08 ± 0.35) × 10 ⁻⁷	
	1214	M8.9	M8III	2.18	0.81	5.95 ± 0.34	2.25 ± 1.02	(1.45 ± 0.13) × 10 ⁻⁷	
	1251	M9.4	M8III	278.96	0.75	6.01 ± 0.35	2.08 ± 0.97	(1.24 ± 0.11) × 10 ⁻⁷	1.29 × 10 ⁻⁷
	1277	M9.7	M8III	241.15	1.15	6.55 ± 0.34	2.06 ± 1.17	(1.22 ± 0.14) × 10 ⁻⁷	
IRC+30055	1215	M7.9	M7III	31.15	0.58	2.19 ± 0.30	2.41 ± 0.31	(1.91 ± 4.07) × 10 ⁻⁷	1.66 × 10 ⁻⁷
IRC+30292	1074	M8.6	M9III	1.88	0.08	3.39 ± 0.34	2.12 ± 0.41	(1.11 ± 0.40) × 10 ⁻⁷	1.35 × 10 ⁻⁷
	1215	M9.6	M8III	156.50	0.50	7.78 ± 0.36	1.99 ± 1.83	(1.13 ± 0.21) × 10 ⁻⁷	8.71 × 10 ⁻⁸
IRC+30515	1215	M7.9	M7III	32.94	0.70	1.43 ± 0.29	4.18 ± 0.46	(5.76 ± 0.93) × 10 ⁻⁷	5.62 × 10 ⁻⁷
IRC+40004	1215	M9.1	M9.5III	8.38	12.28	1.05 ± 0.33	2.41 ± 0.25	(1.33 ± 0.19) × 10 ⁻⁷	
	1251	M9.0	M9.5III	10.62	8.52	1.33 ± 0.33	2.25 ± 0.24	(1.16 ± 0.18) × 10 ⁻⁷	3.09 × 10 ⁻⁷
IRC+40442	1251	M9.3	M8III	355.87	1.49	4.84 ± 0.33	3.89 ± 1.16	(4.33 ± 0.25) × 10 ⁻⁷	
IRC+40448	1215	M7.0	M9.5III	204.46	14.00	2.96 ± 0.34	4.43 ± 0.73	(4.51 ± 0.13) × 10 ⁻⁷	2.34 × 10 ⁻⁶
IRC+40485	1215	c	M2III	350.92	6.39	8.48 ± 0.34	2.97 ± 5.78	(6.89 ± 2.69) × 10 ⁻⁷	3.39 × 10 ⁻⁷
	1251	c	M2III	388.18	6.13	8.12 ± 0.33	3.13 ± 5.23	(7.68 ± 2.56) × 10 ⁻⁷	
IRC+50096	1215	c	M2III	463.34	8.76	6.90 ± 0.33	3.30 ± 3.50	(8.53 ± 1.80) × 10 ⁻⁷	7.41 × 10 ⁻⁷
	1251	c	M2III	425.89	8.06	7.23 ± 0.33	3.70 ± 4.42	(1.07 ± 0.26) × 10 ⁻⁶	
IRC+50260	1054	M7.0	M6.5III	2.45	0.30	0.24 ± 0.29	1.54 ± 0.14	(8.40 ± 9.29) × 10 ⁻⁸	
IRC+50261	1078	M6.0	M5.5III	2.35	0.28	0.00 ± 0.26	1.23 ± 0.11	(6.12 ± 0.06) × 10 ⁻⁸	
IRC+50357	1215	c	M9.5III	89.99	14.10	4.72 ± 0.37	1.25 ± 0.35	(3.61 ± 0.20) × 10 ⁻⁸	1.48 × 10 ⁻⁷
IRC+60015	1251	M7.8	M7III	40.14	0.35	1.33 ± 0.29	2.85 ± 0.31	(2.67 ± 4.16) × 10 ⁻⁷	
IRC+60052	1251	M6.0	M5.5III	1.63	0.17	2.32 ± 0.27	2.44 ± 0.33	(2.40 ± 0.55) × 10 ⁻⁷	
IRC+60092	1215	M8.6	M9III	2.00	0.13	3.24 ± 0.33	3.94 ± 0.69	(3.83 ± 0.12) × 10 ⁻⁷	5.75 × 10 ⁻⁷
IRC+60169	1054	M9.3	M8III	347.40	0.26	4.81 ± 0.35	5.35 ± 1.71	(8.19 ± 0.51) × 10 ⁻⁷	
IRC+60184	1054	M8.8	M8.5III	18.37	0.27	0.00 ± 0.32	1.75 ± 0.16	(8.14 ± 0.85) × 10 ⁻⁸	
	1106	M9.3	M8III	496.80	0.49	2.13 ± 0.39	2.12 ± 0.33	(1.28 ± 0.36) × 10 ⁻⁷	
IRC+60288	1214	M8.2	M7III	17.24	0.53	0.58 ± 0.30	2.33 ± 0.23	(1.79 ± 0.22) × 10 ⁻⁷	
IRC+60289	1251	M8.2	M7.5III	20.50	0.48	0.91 ± 0.31	2.50 ± 0.25	(1.92 ± 0.27) × 10 ⁻⁷	2.29 × 10 ⁻⁷
	1215	M7.9	M7III	32.03	0.78	1.95 ± 0.29	1.75 ± 0.22	(1.01 ± 1.96) × 10 ⁻⁷	
IRC+60316	1215	M6.0	M6III	2.52	0.28	2.75 ± 0.28	2.68 ± 0.41	(2.70 ± 0.73) × 10 ⁻⁷	1.95 × 10 ⁻⁷
IRC+60334	1251	M8.9	M8.5III	1.96	0.14	2.37 ± 0.33	2.58 ± 0.35	(1.78 ± 0.41) × 10 ⁻⁷	
IRC+70102	1052	M9.0	M8III	8.50	0.29	1.82 ± 0.34	1.86 ± 0.23	(9.86 ± 0.20) × 10 ⁻⁸	1.20 × 10 ⁻⁷
IRC+70171	1215	M9.3	M8III	308.81	0.88	5.24 ± 0.34	2.95 ± 1.03	(2.49 ± 0.17) × 10 ⁻⁷	1.45 × 10 ⁻⁷
	1251	M9.2	M8III	11.22	0.34	5.23 ± 0.34	2.60 ± 0.90	(1.93 ± 1.31) × 10 ⁻⁷	1.86 × 10 ⁻⁷
IRC+80005	1050	M9.2	M8III	28.41	2.07	4.43 ± 0.33	2.42 ± 0.62	(1.67 ± 0.83) × 10 ⁻⁷	1.70 × 10 ⁻⁷
	1215	M9.5	M8III	388.53	2.40	4.42 ± 0.33	2.74 ± 0.70	(2.15 ± 0.11) × 10 ⁻⁷	
R And-A	1214	S-type	M10III	476.42	1.71	4.23 ± 0.30	8.80 ± 2.19	(2.55 ± 0.12) × 10 ⁻⁶	
	1277	S-type	M10III	629.77	1.29	5.67 ± 0.30	6.53 ± 2.75	(1.40 ± 0.12) × 10 ⁻⁶	1.74 × 10 ⁻⁶
W And-A	1215	M8.9	M9III	2.16	0.66	1.09 ± 0.29	6.70 ± 0.69	(1.48 ± 0.21) × 10 ⁻⁶	
	1251	M8.3	M8.5III	24.07	0.73	2.04 ± 0.34	6.52 ± 0.93	(1.40 ± 0.34) × 10 ⁻⁶	
T Aqr-A	1277	M7.9	M8III	29.15	2.30	2.89 ± 0.31	6.58 ± 1.03	(1.33 ± 0.37) × 10 ⁻⁶	
	1302	M6.5	M6.5III	5.25	0.12	2.15 ± 0.39	5.91 ± 0.95	(9.30 ± 0.27) × 10 ⁻⁷	1.58 × 10 ⁻⁶
T Ari-A	1251	M8.0	M8III	40.41	0.88	0.00 ± 0.27	1.10 ± 0.09	(4.26 ± 0.39) × 10 ⁻⁸	
U Ari-A	1214	M7.0	M7III	3.32	0.22	0.60 ± 0.27	5.54 ± 0.50	(1.16 ± 0.13) × 10 ⁻⁶	1.26 × 10 ⁻⁶
	1251	M9.5	M9.5III	478.73	1.48	1.24 ± 0.33	3.05 ± 0.31	(2.66 ± 0.40) × 10 ⁻⁷	
R Boo-A	1277	mid M?	M9.5III	948.13	0.80	0.43 ± 0.36	2.92 ± 0.27	(2.44 ± 0.30) × 10 ⁻⁷	
R Cam-A	1078	M8.1	M8III	17.42	0.54	0.00 ± 0.30	2.29 ± 0.20	(1.61 ± 0.17) × 10 ⁻⁷	
R Cas-A	1078	S-type	M10III	1169.95	0.49	0.71 ± 0.23	1.66 ± 0.15	(1.34 ± 0.16) × 10 ⁻⁷	
	1214	M9.7	M9.5III	394.35	1.77	3.86 ± 0.33	15.35 ± 3.24	(6.74 ± 0.27) × 10 ⁻⁶	
	1251	M9.9	M10III	423.20	1.18	3.86 ± 0.34	13.35 ± 2.81	(5.10 ± 0.20) × 10 ⁻⁶	
	1302	M9.3	M9.5III	428.99	1.09	4.44 ± 0.41	14.06 ± 4.95	(5.65 ± 0.39) × 10 ⁻⁶	6.03 × 10 ⁻⁶
T Cas-A	1214	M8.9	M9III	18.51	1.96	3.09 ± 0.32	10.68 ± 1.76	(3.26 ± 0.97) × 10 ⁻⁶	3.02 × 10 ⁻⁶
	1251	M8.7	M8III	13.98	1.54	2.44 ± 0.31	10.70 ± 1.46	(3.52 ± 0.81) × 10 ⁻⁶	
V Cas-A	1214	M7.9	M8III	31.07	0.61	0.86 ± 0.29	4.55 ± 0.45	(6.83 ± 0.89) × 10 ⁻⁷	7.41 × 10 ⁻⁷
Y Cas-A	1214	M8.1	M8III	21.31	0.47	0.59 ± 0.30	4.22 ± 0.41	(5.85 ± 0.72) × 10 ⁻⁷	7.41 × 10 ⁻⁷
SS Cas-A	1277	M4.0	M4III	3.44	0.68	0.00 ± 0.20	1.35 ± 0.11	(8.93 ± 0.71) × 10 ⁻⁸	
T Cep-A	1214	M8.6	M8III	11.20	1.42	1.55 ± 0.31	14.37 ± 1.58	(6.35 ± 0.11) × 10 ⁻⁶	
R Cyg-A	1214	S-type	M10III	1056.44	0.56	0.76 ± 0.23	4.14 ± 0.38	(7.88 ± 0.93) × 10 ⁻⁷	
X Cyg-A	1214	M8.2	M8III	15.39	0.71	0.77 ± 0.31	14.84 ± 1.44	(6.77 ± 0.87) × 10 ⁻⁶	
S Lac-A	1251	M8.2	M8III	16.18	0.95	0.93 ± 0.30	2.16 ± 0.21	(1.43 ± 0.19) × 10 ⁻⁷	1.70 × 10 ⁻⁷
W Lyr-A	1214	M6.5	M6.5III	13.15	0.21	0.00 ± 0.26	1.33 ± 0.11	(6.66 ± 0.62) × 10 ⁻⁸	
V Mon-A	1277	M5.0	M5III	2.24	0.42	0.78 ± 0.24	4.78 ± 0.44	(9.84 ± 0.12) × 10 ⁻⁷	
R Tri-A	1214	M7.0	M7III	3.52	0.85	0.00 ± 0.20	4.09 ± 0.33	(8.16 ± 0.64) × 10 ⁻⁷	
	1251	M5.5	M5.5III	8.62	0.79	0.00 ± 0.23	4.51 ± 0.37	(8.73 ± 0.75) × 10 ⁻⁷	
W Peg-A	1277	M5.0	M5III	13.95	0.43	0.00 ± 0.27	4.67 ± 0.40	(7.68 ± 0.71) × 10 ⁻⁷	9.33 × 10 ⁻⁷
	1214	M8.9	M9III	15.10	1.69	2.96 ± 0.32	7.32 ± 1.17	(1.65 ± 0.47) × 10 ⁻⁶	1.45 × 10 ⁻⁶
Z Peg-A	1214	M8.5	M8.5III	19.11	1.75	2.39 ± 0.31	4.18 ± 0.57	(5.37 ± 0.12) × 10 ⁻⁷	5.01 × 10 ⁻⁷

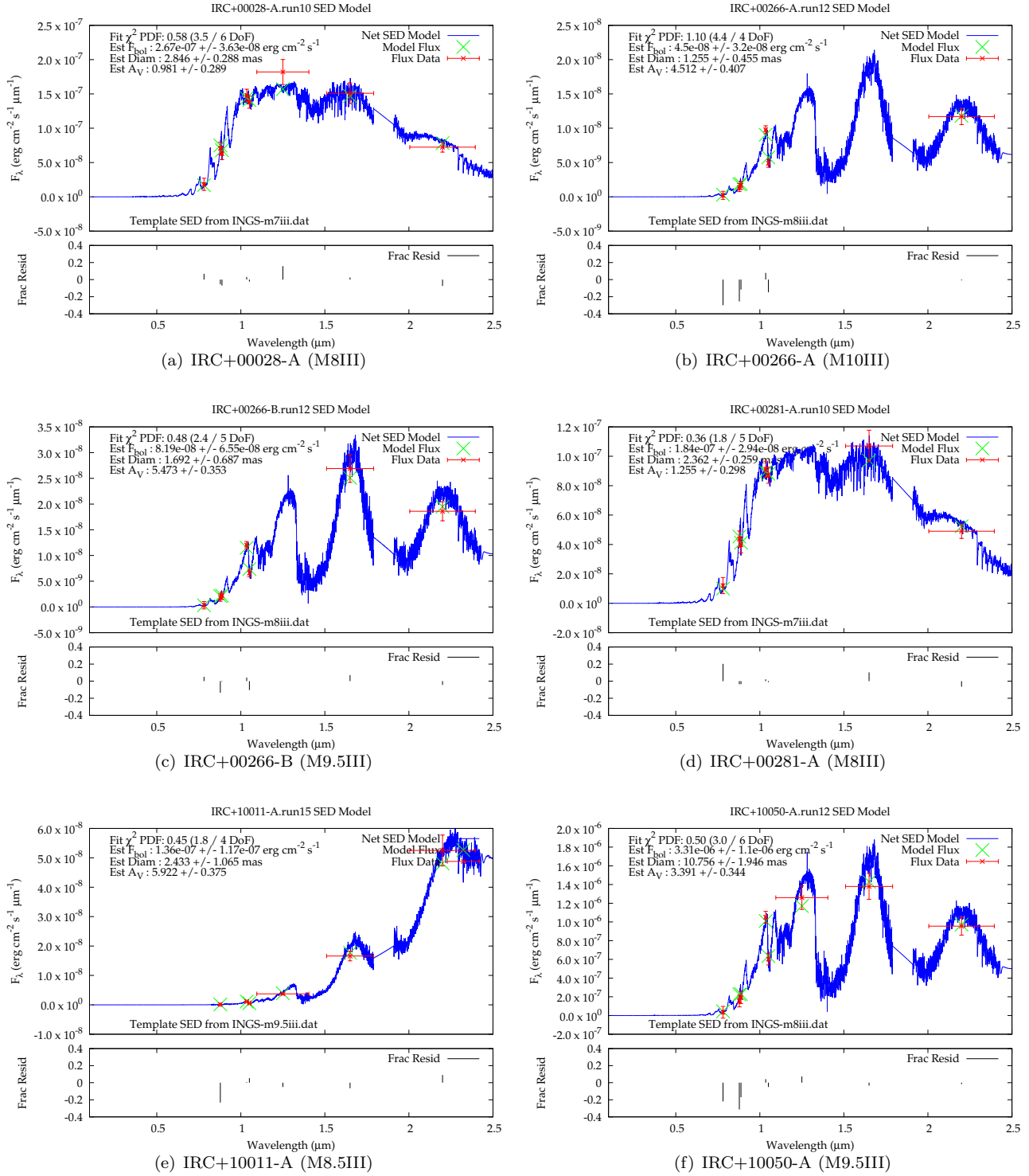


FIG. A1.— SED fits as described in §2.2.

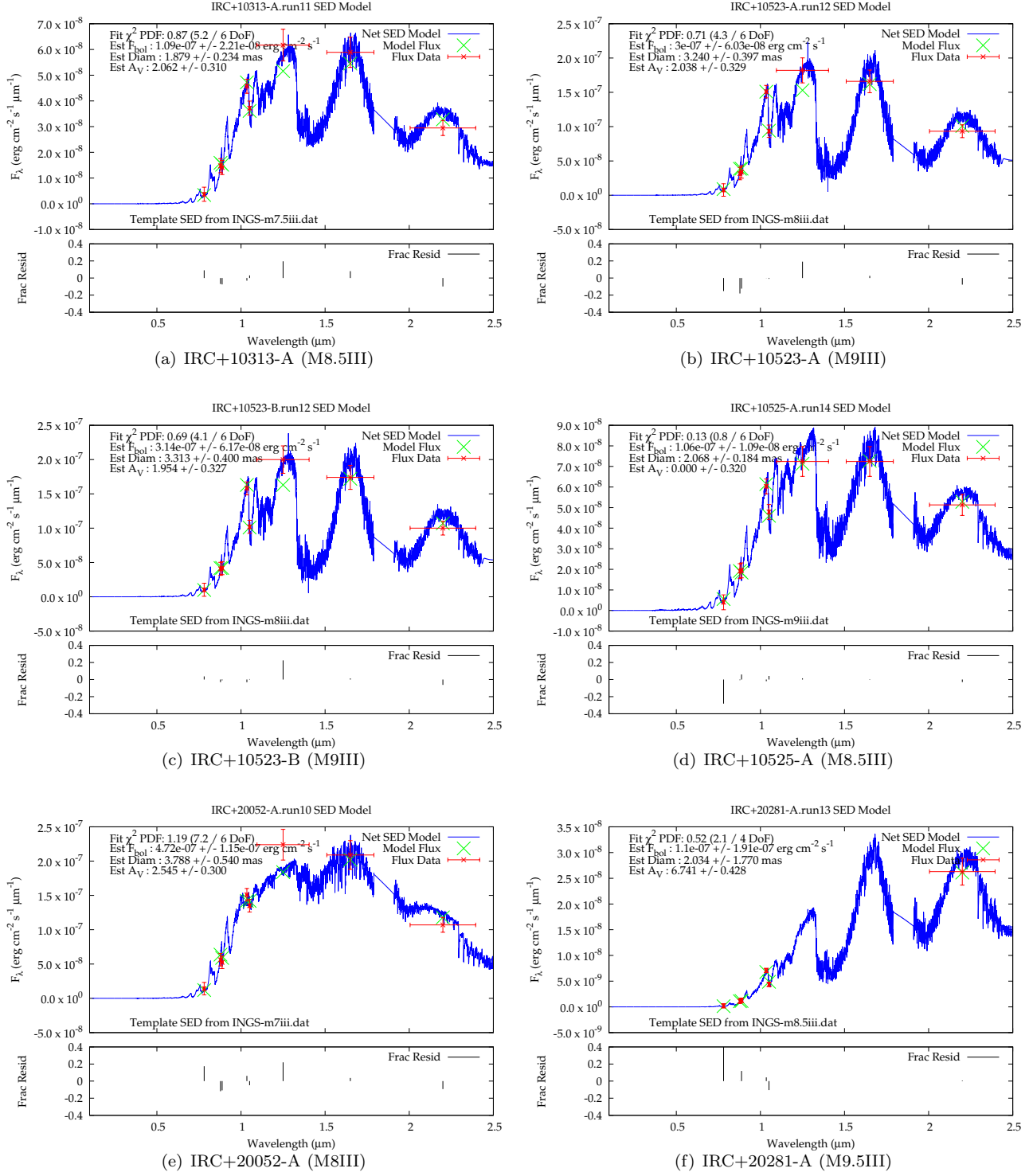


FIG. A2.— SED fits as described in §2.2.

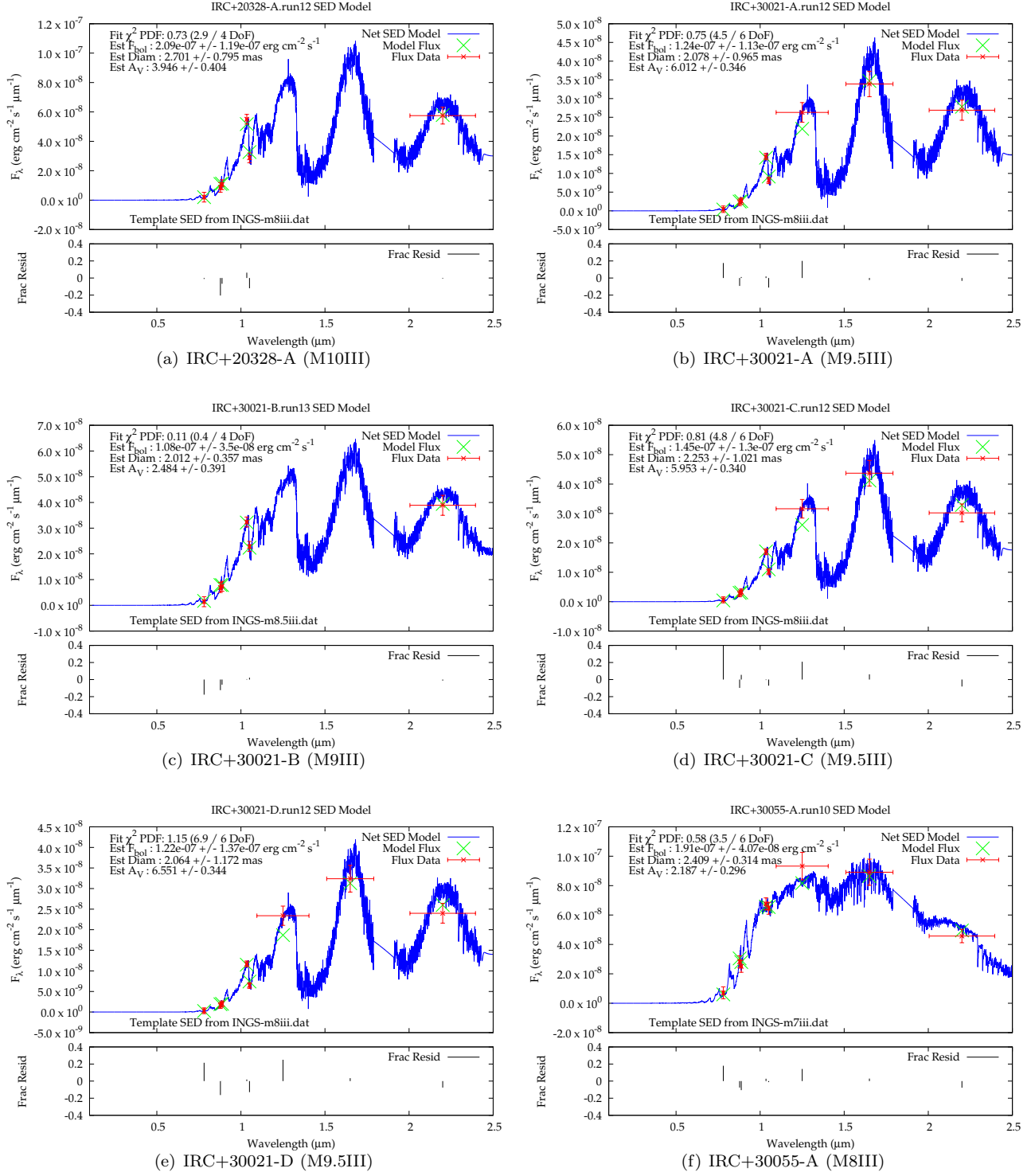


FIG. A3.— SED fits as described in §2.2.

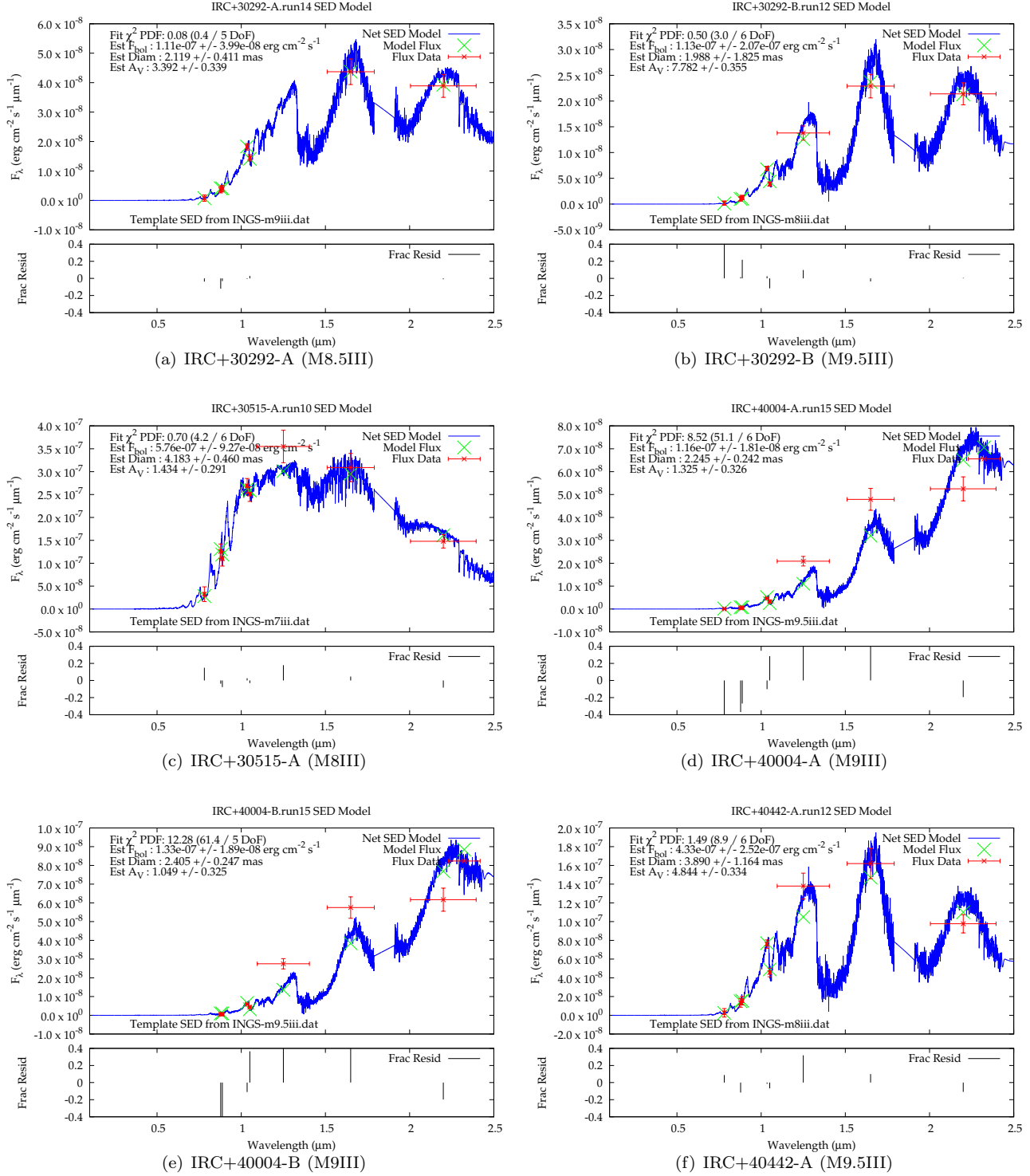


FIG. A4.— SED fits as described in §2.2.

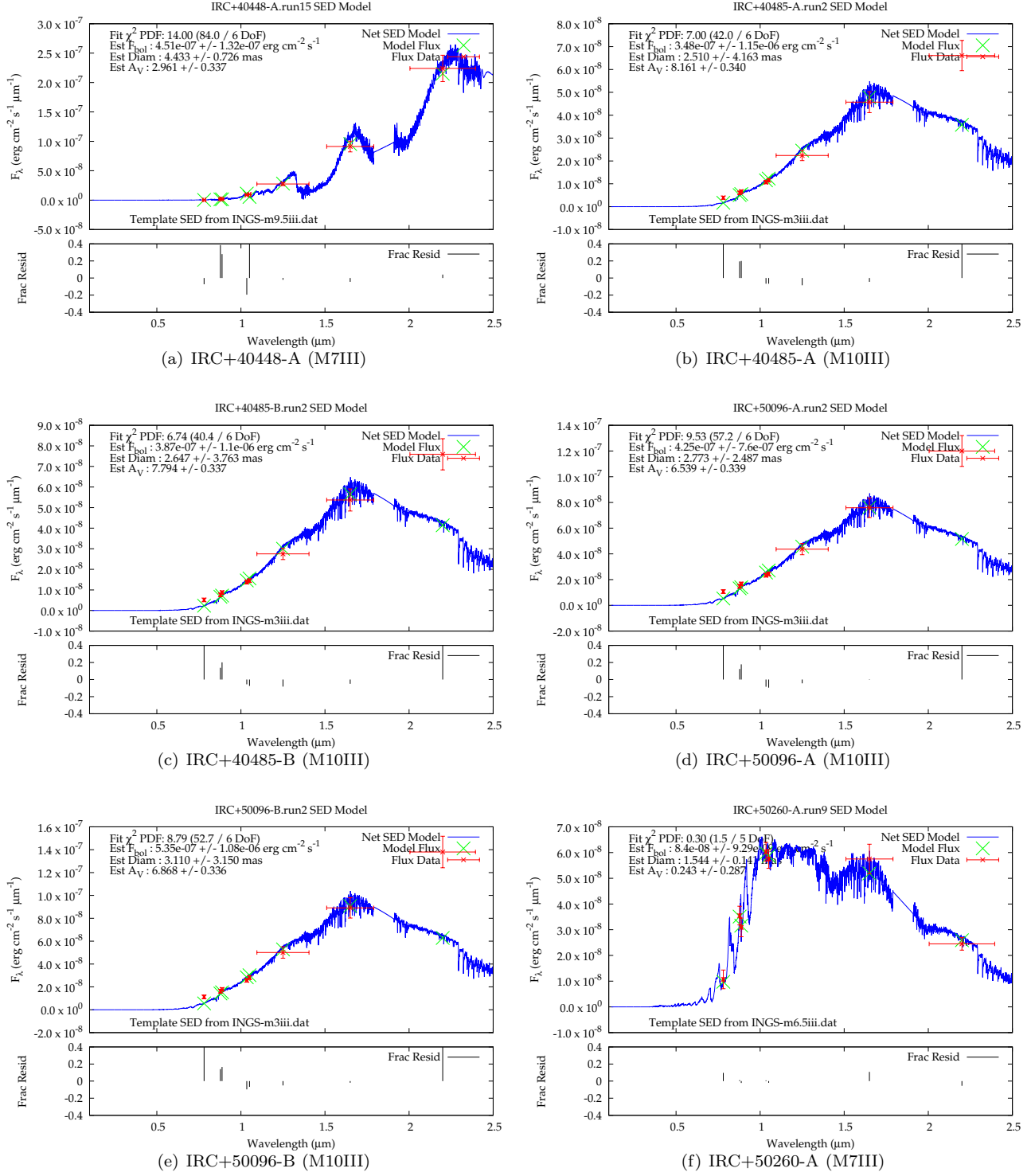


FIG. A5.— SED fits as described in §2.2.

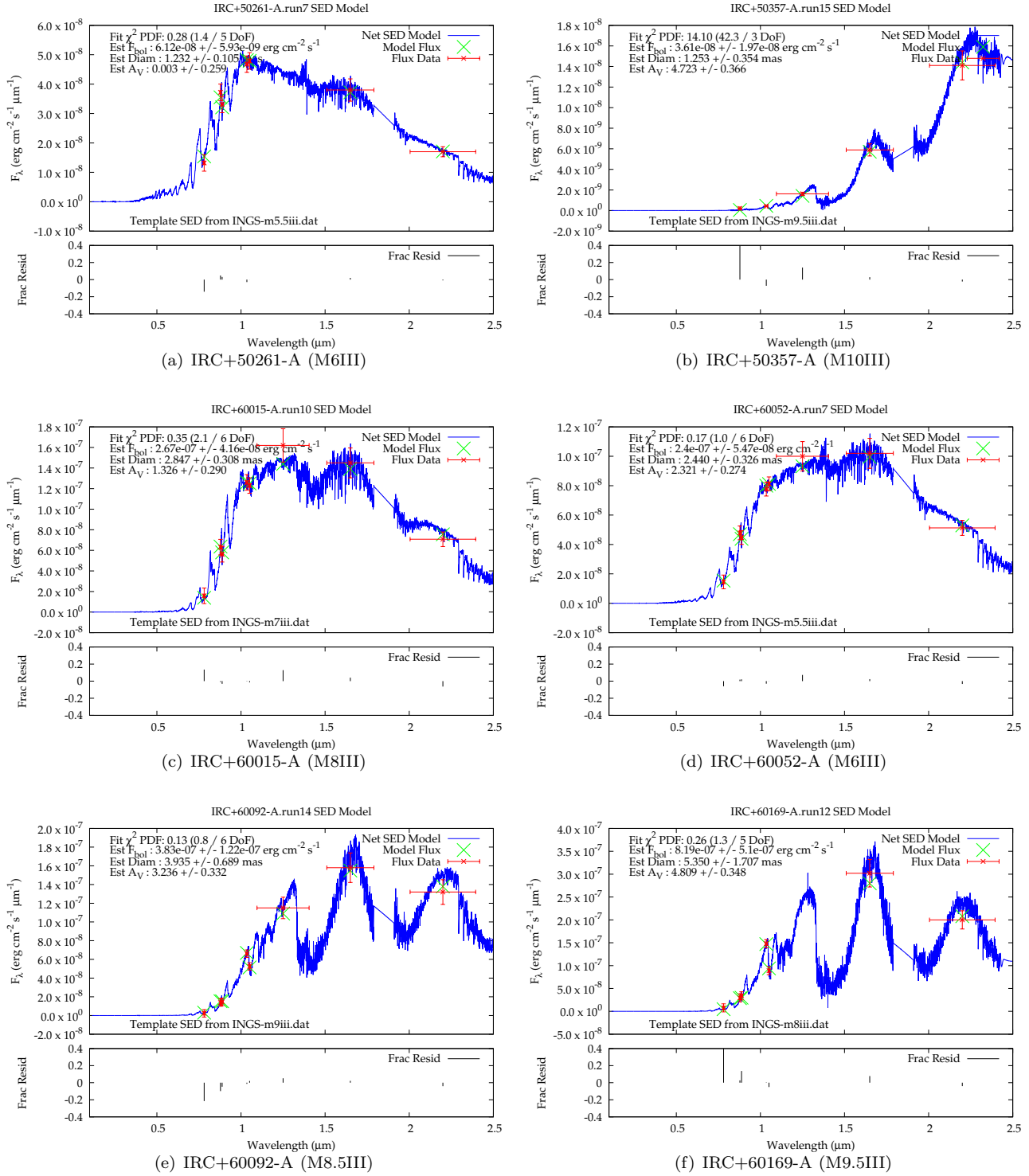


FIG. A6.— SED fits as described in §2.2.

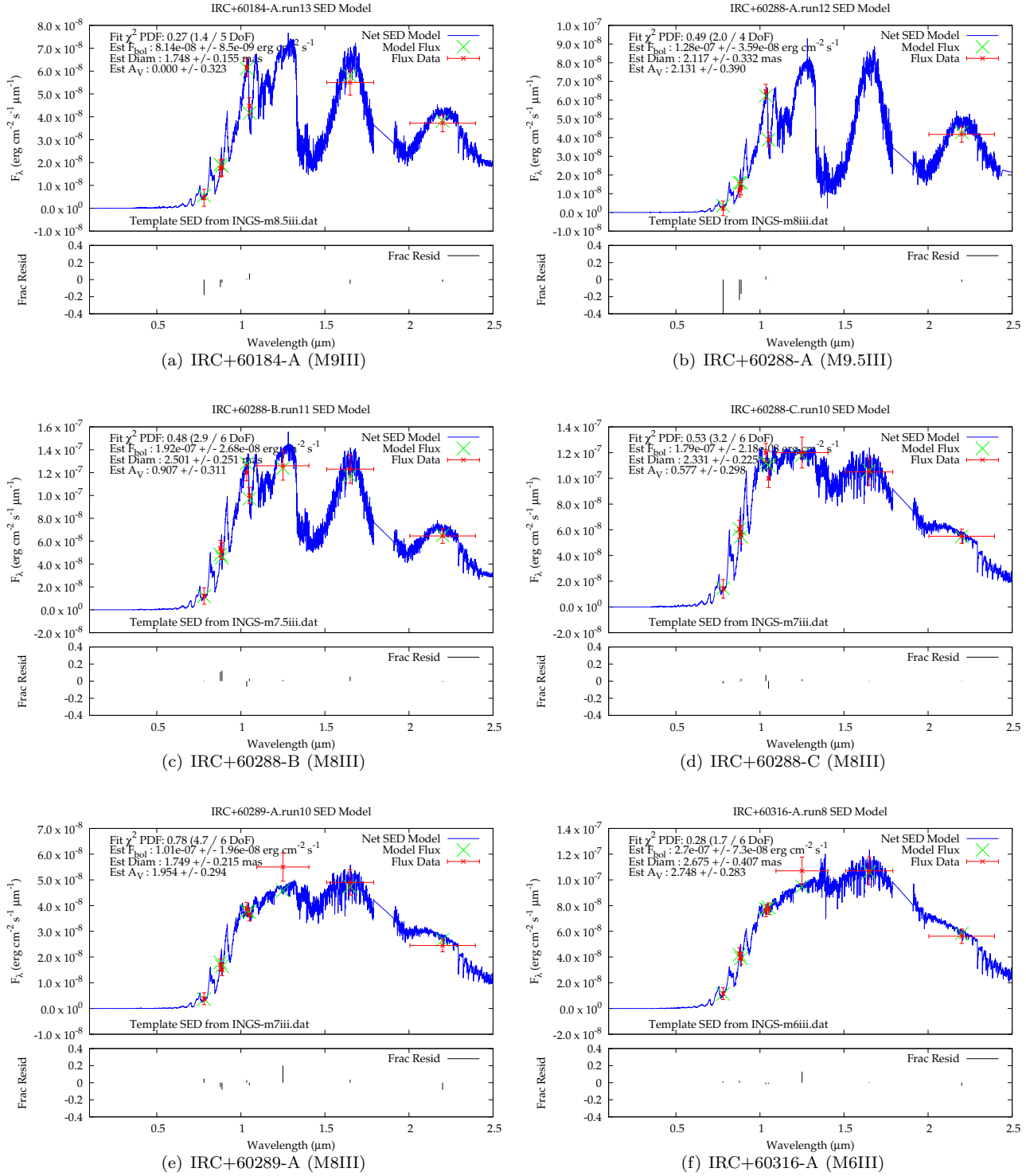


FIG. A7.— SED fits as described in §2.2.

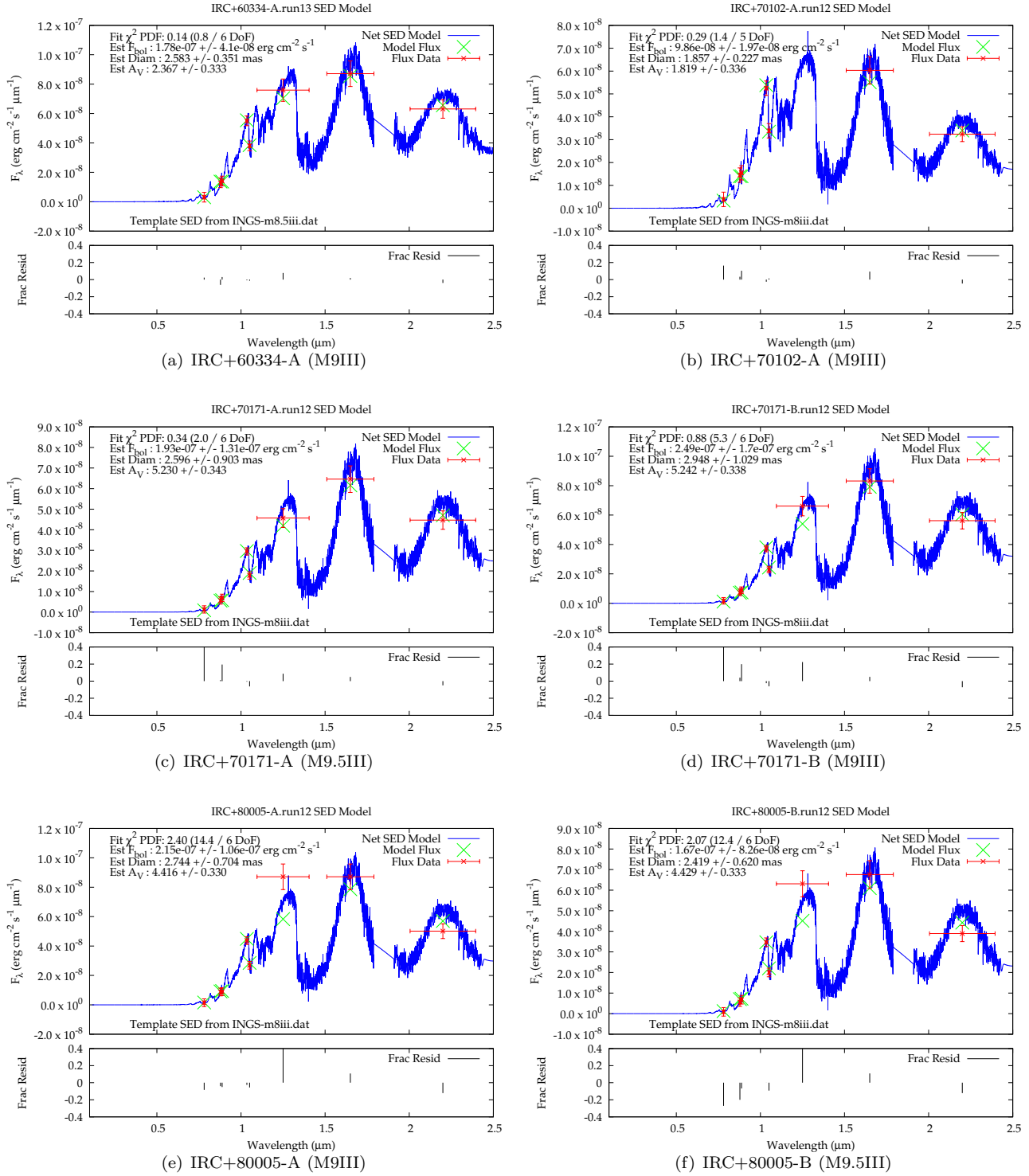


FIG. A8.— SED fits as described in §2.2.

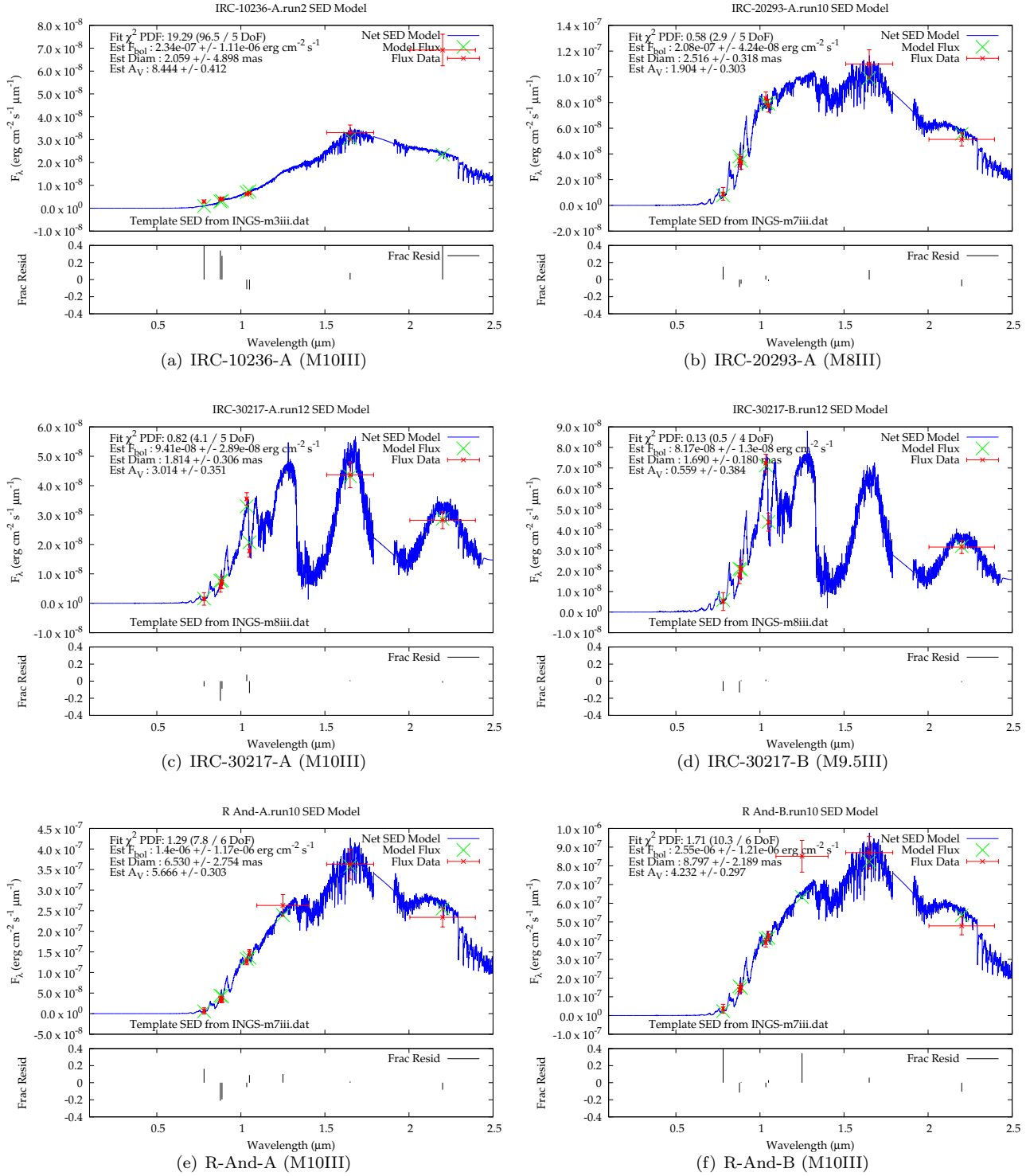


FIG. A9.— SED fits as described in §2.2.

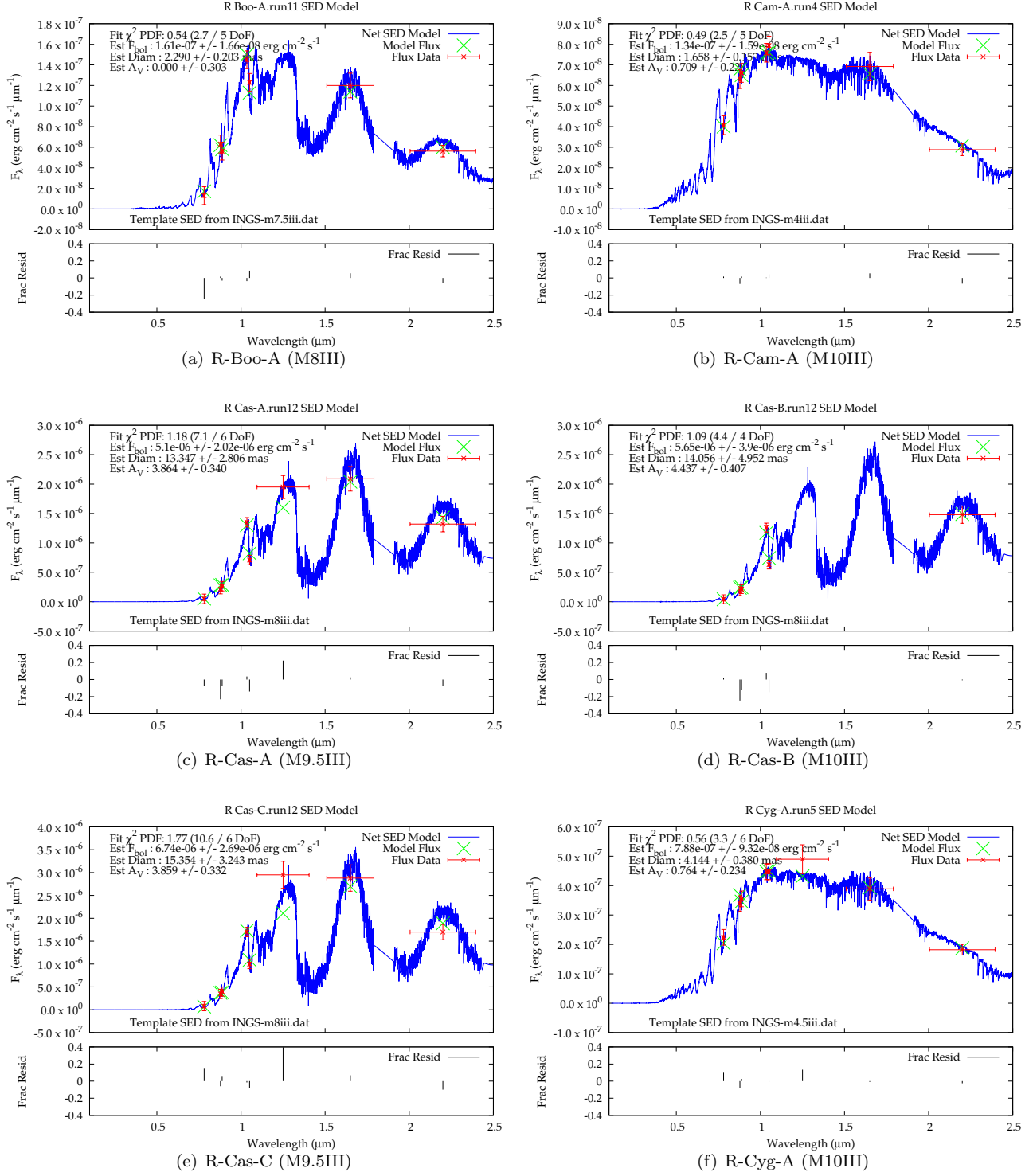


FIG. A10.— SED fits as described in §2.2.

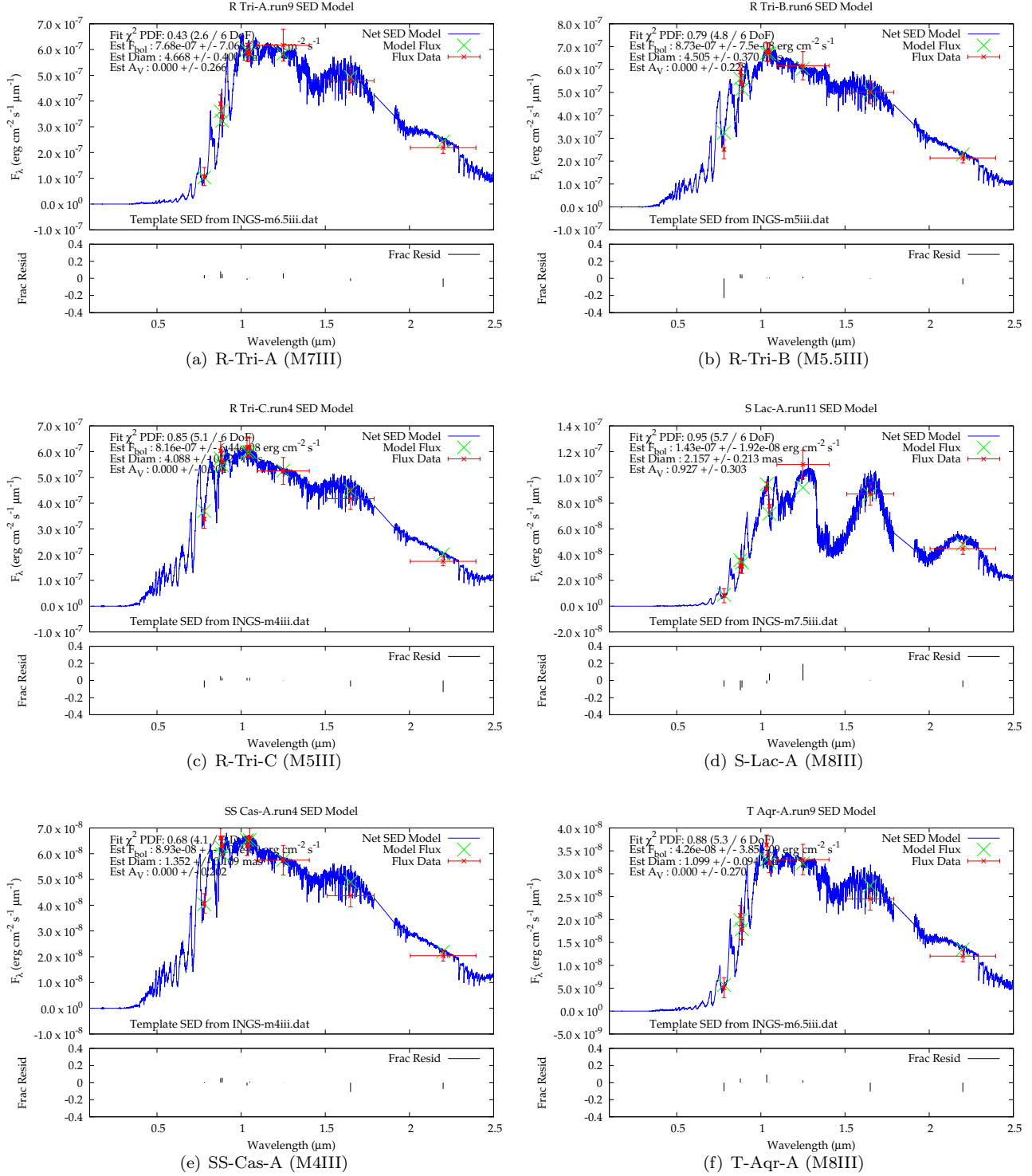


FIG. A11.— SED fits as described in §2.2.

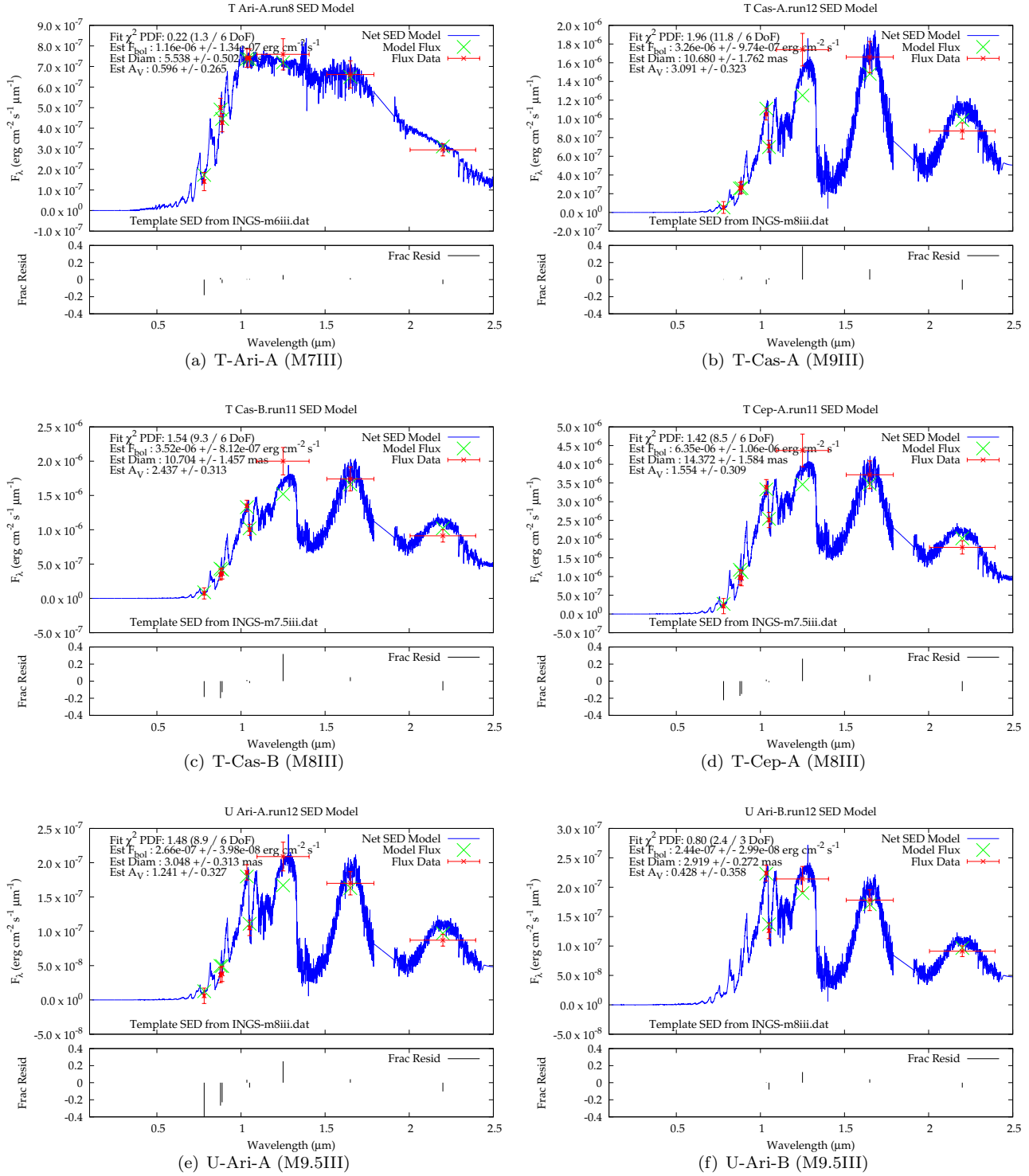


FIG. A12.— SED fits as described in §2.2.

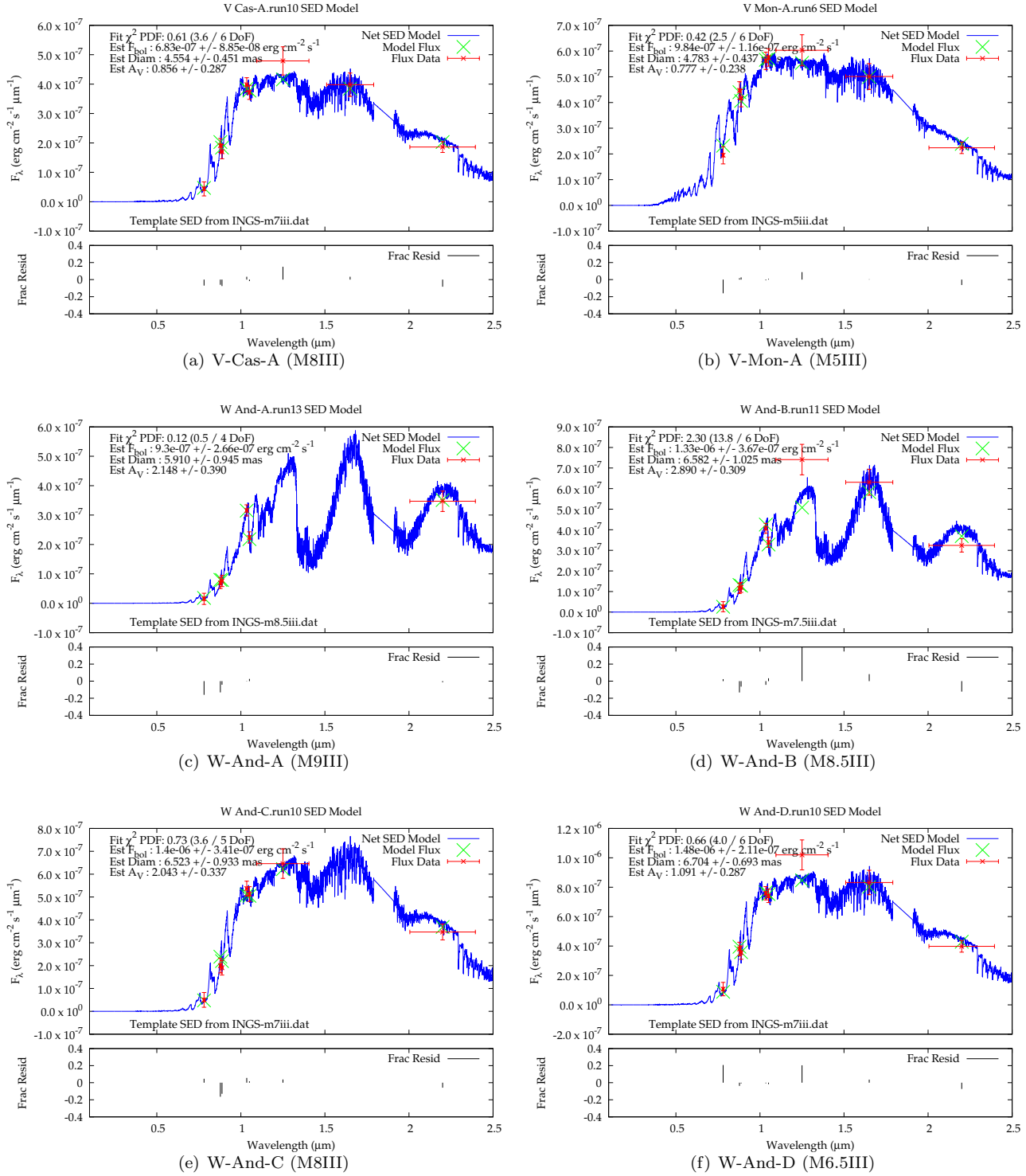


FIG. A13.— SED fits as described in §2.2.

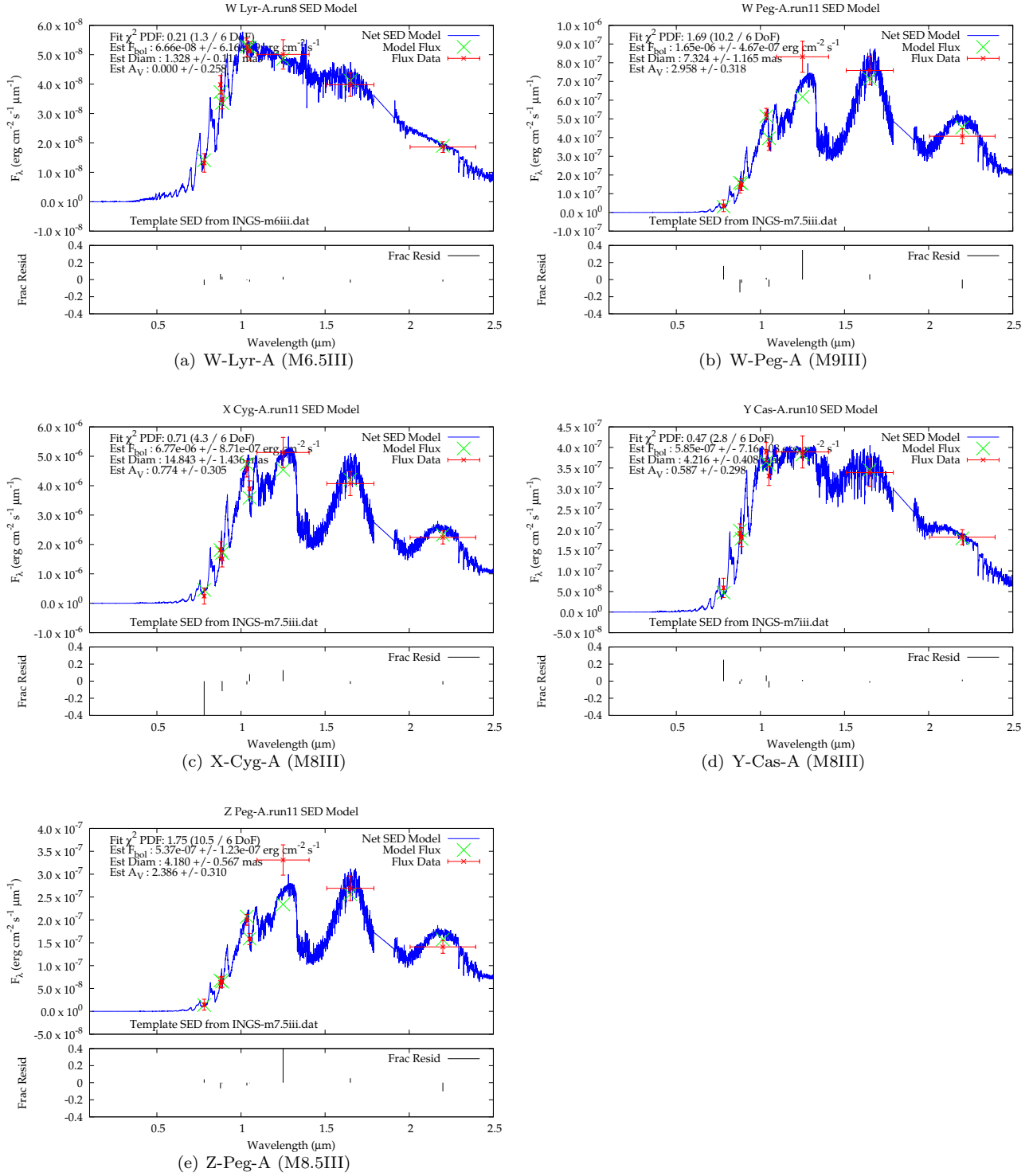


FIG. A14.— SED fits as described in §2.2.